INTERNATIONAL ATOMIC ENERGY AGENCY
UNITED NATIONS EDUCATIONAL, SCIENTIFIC AND CULTURAL ORGANIZATION
INTERNATIONAL CENTRE FOR THEORETICAL PHYSICS
I.C.T.P., P.O. BOX 586, 34100 TRIESTE, ITALY, CABLE: CENTRATOM TRIESTE

UNITED NATIONS INDUSTRIAL DEVELOPMENT ORGANIZATION

INTERNATIONAL CENTRE FOR SCIENCE AND HIGH TECHNOLOGY
c/o INTERNATIONAL CENTRE FOR THEORETICAL PHYSICS 34100 TRIESTE (ITALY) VIA GRIGNANO, 9 (ADRIATICO PALACE) P.O. BOX 586 TELEPHONE 040-224572 TELEFAX 040-224575 TELEX 460449 APH I

SMR/543 - 19

EXPERIMENTAL WORKSHOP ON HIGH TEMPERATURE SUPERCONDUCTORS AND RELATED MATERIALS (BASIC ACTIVITIES)

(11 February - 1 March 1991)

" EPR Spectroscopy and Microwave Absorption of HTS Materials "

PART I

presented by:

G. AMORETTI
Università degli Studi di Parma
Dipartimento di Fisica
Viale delle Scienze
43100 Parma
Italy

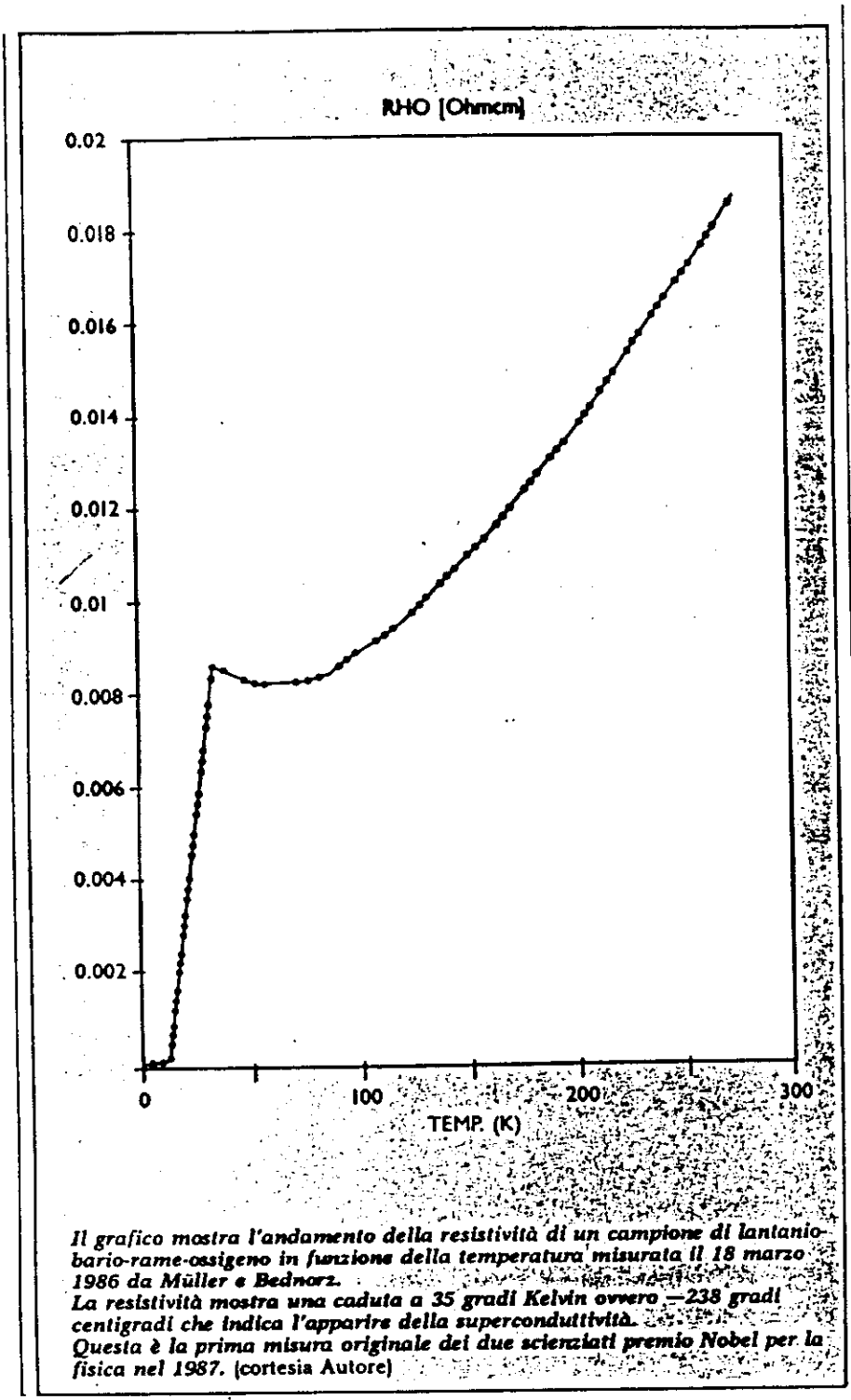

Il grafico mostra l'andamento della resistività di un campione di lantanio-bario-rame-ossigeno in funzione della temperatura misurata il 18 marzo 1986 da Müller e Bednorz.
La resistività mostra una caduta a 35 gradi Kelvin ovvero —238 gradi centigradi che indica l'apparire della superconduttività.
Questa è la prima misura originale dei due scienziati premio Nobel per la fisica nel 1987. (cortesia Autore)

Since the discovery of ... by ...

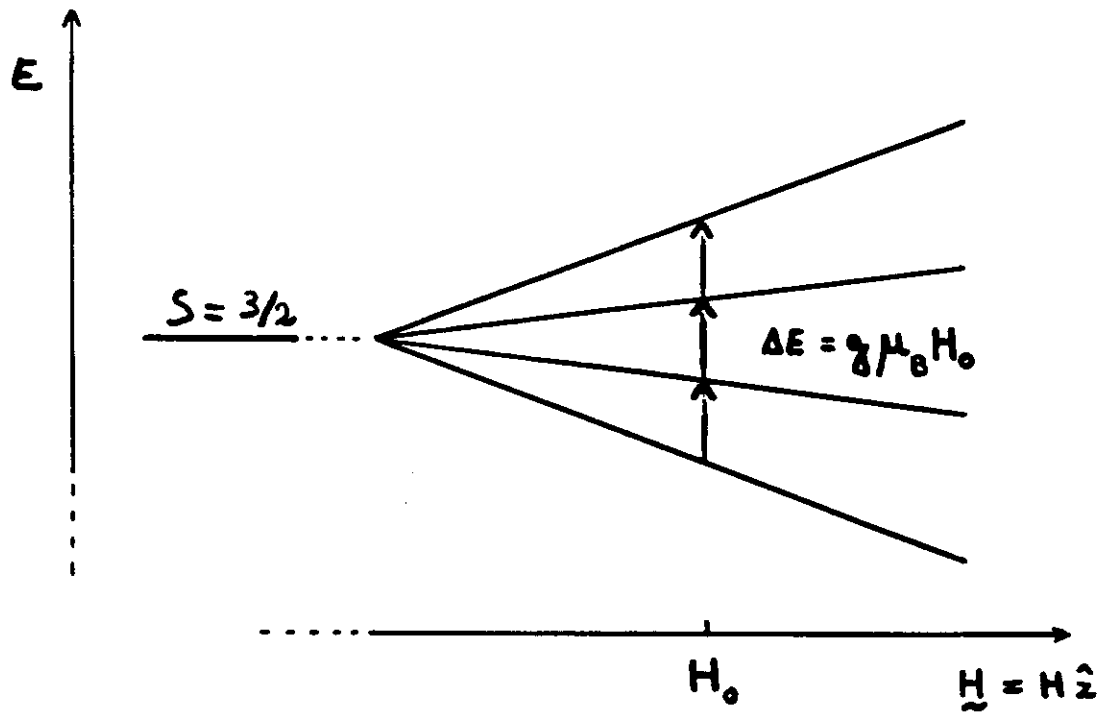

$\underset{\sim}{H}_t = H_t \cos \omega t$;
$H_t \ll H$

$$\boxed{h\nu = g \mu_B H_0}$$

$\mu_B = 1.4$ MHz/gauss , $g = 2$

	ν	λ	H_0
X band	~ 9 GHz	~ 3 cm	~ 3200 gauss
Q band	~ 35 GHz	~ 0.8 cm	~ 12500 gauss

T_1 : spin - lattice

T_2 : spin - spin

$T_1 \gtrsim T_2 \sim 10^{-9}$ sec

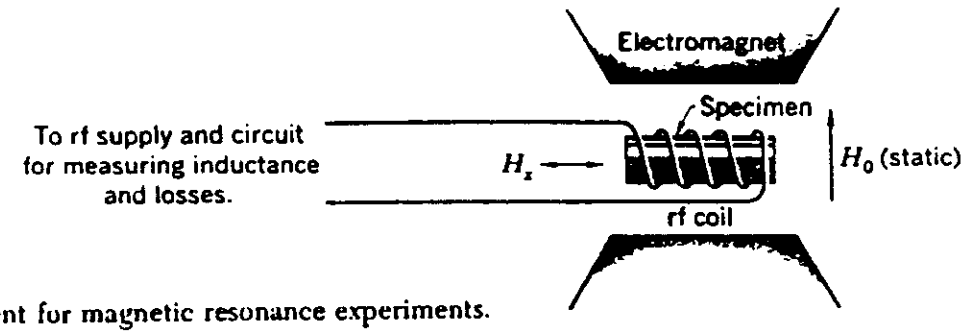

Schematic arrangement for magnetic resonance experiments.

$$dM_z/dt = \gamma(\mathbf{M} \times \mathbf{H})_z + (M_0 - M_z)/T_1,$$

$$dM_x/dt = \gamma(\mathbf{M} \times \mathbf{H})_x - M_x/T_2;$$
$$dM_y/dt = \gamma(\mathbf{M} \times \mathbf{H})_y - M_y/T_2,$$

$$\hbar\gamma = g\mu_B$$

$H_x \ll H_0$

$$M_x(t) = [\chi' \cos\omega t + \chi'' \sin\omega t] H_{x0}$$

$$\chi' = \frac{\chi_0}{2} \omega_0 T_2 \frac{(\omega_0 - \omega) T_2}{1 + (\omega - \omega_0)^2 T_2^2}$$

$$\chi'' = \frac{\chi_0}{2} \omega_0 T_2 \frac{1}{1 + (\omega - \omega_0)^2 T_2^2}$$

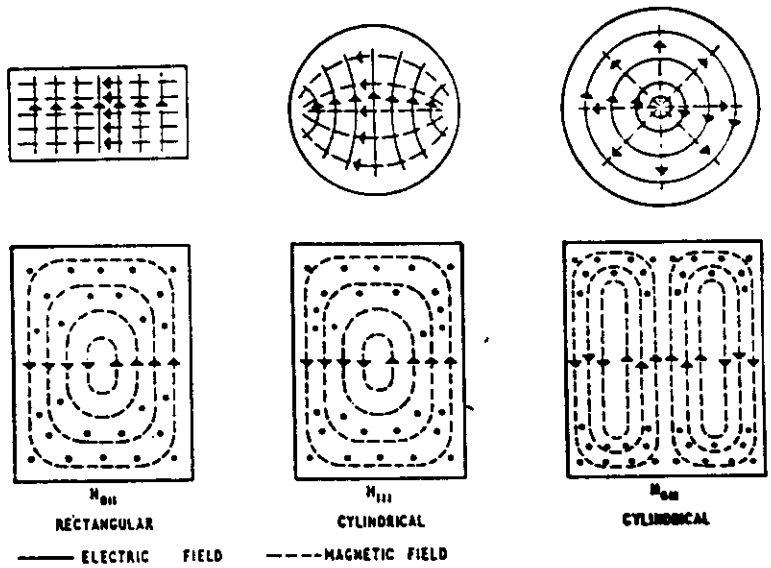

Fig. 10.1. Some commonly used microwave cavities, showing the electric and magnetic field configurations

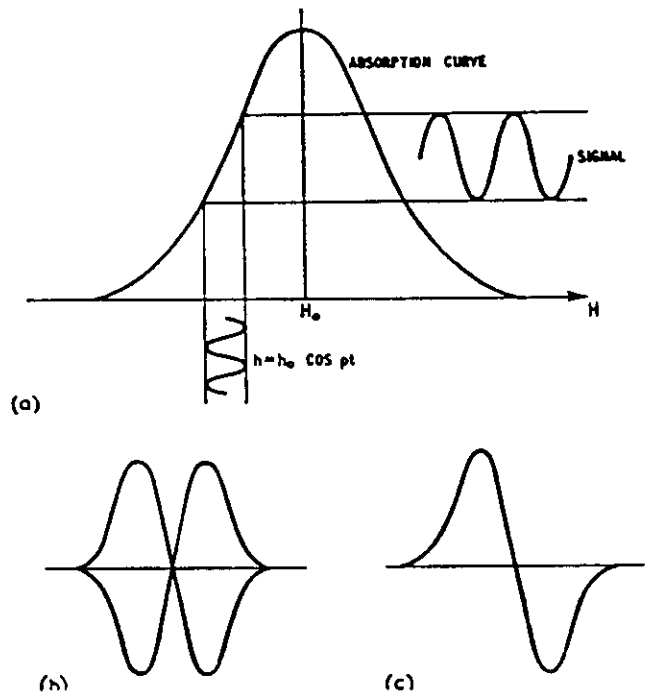

Fig. 10.9. Outline of the signal produced by a high frequency modulation system. (*a*) The origin of the signal, (*b*) the unrectified signal, (*c*) the output of a phase-sensitive rectifier

gruppo del ferro : $\ldots 3d^N 4s^2$

terre rare : $\ldots 4f^N 5s^2 5p^6 5d^1 6s^2$

attinidi : $\ldots 5f^N 6s^2 6p^6 6d^1 7s^2$

cm^{-1}	3d	4f	5f
Coulomb energy	$10^4 \sim 10^5$	$10^4 \sim 10^5$	$10^4 \sim 10^5$
S-O splitting	$10^2 \sim 10^3$	10^3	3×10^3
C F splitting	10^4	$10^1 \sim 10^2$	$10^2 \sim 10^3$

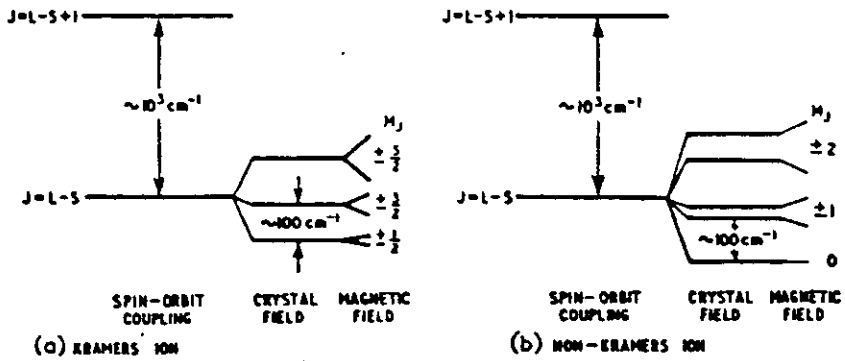

Energy level diagrams to illustrate typical behaviour of (*a*) a Kramers and (*b*) a non-Kramers ion in a 'weak' crystal field (splittings not to scale)

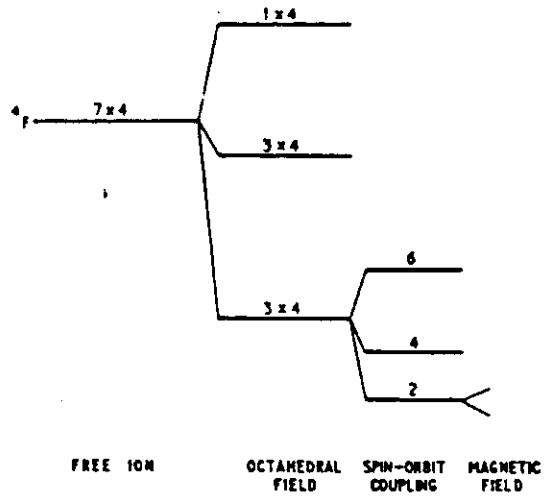

Splitting of the ^4F levels in Co^{2+} due to the combined effect of an octahedral crystal field and spin-orbit coupling. The number against each level indicates the degeneracy of that level

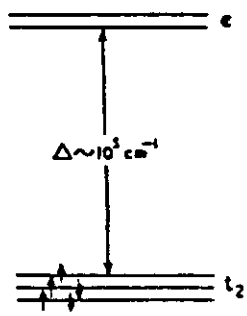

Illustration of the 'strong field' $3d^5$ configuration, all five electrons being in triplet t_2 orbitals and giving rise to a total spin $S = \frac{5}{2}$

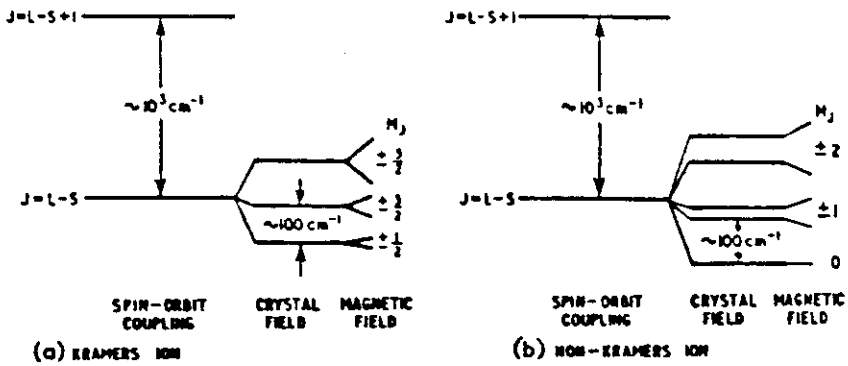

Fig. 2.2. Energy level diagrams to illustrate typical behaviour of (*a*) a Kramers and (*b*) a non-Kramers ion in a 'weak' crystal field (splittings not to scale)

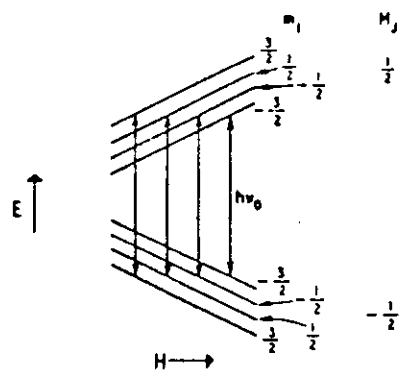

Fig. 2.6. Diagram to show the origin of hyperfine structure for the case $M_J = \frac{1}{2}$, $m_I = \frac{3}{2}$. The four allowed transitions (characterised by $\Delta m_I = 0$) are indicated

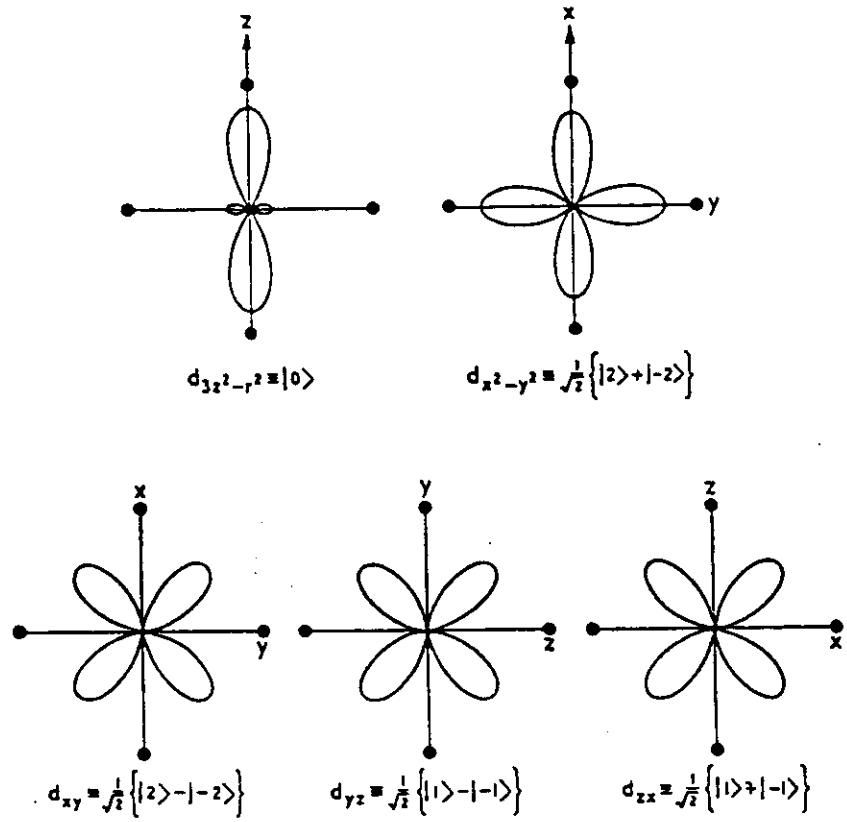

Angular distribution functions for the five *d* orbitals
The black circles represent neighbouring ions

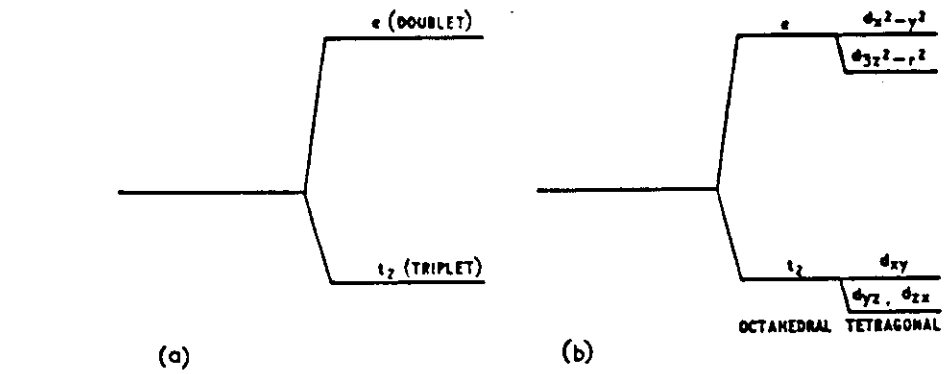

Energy levels of a single *d* electron in crystal fields of
(*a*) octahedral and (*b*) tetragonal symmetry

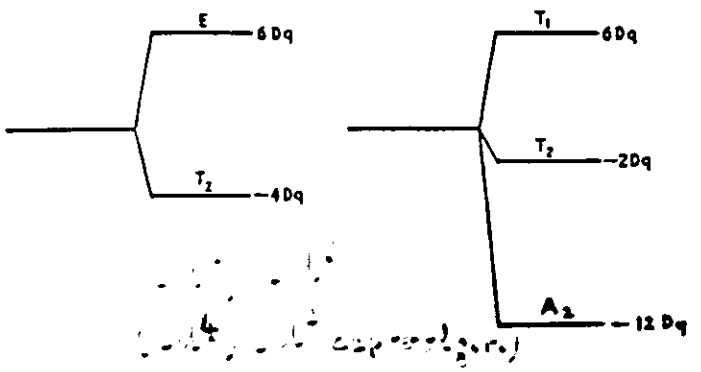

The splitting of *D* and *F* states in octahedral crystal field

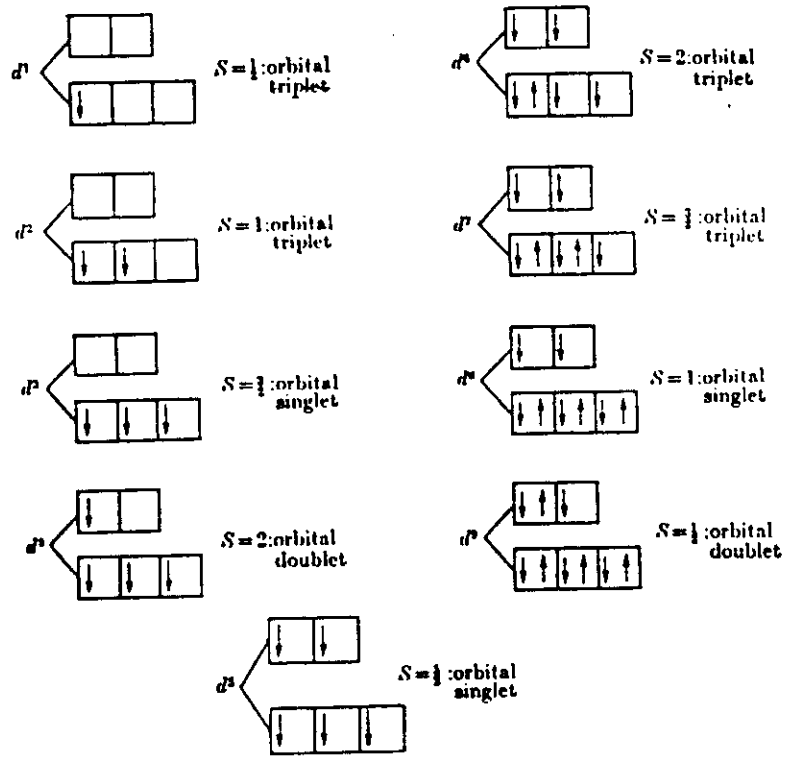

FIG. 7.7. Construction of the ground states of the d-configurations in an octahedral field using the strong crystal field approach, but assuming the spin coupling to be stronger than the crystal field energy.

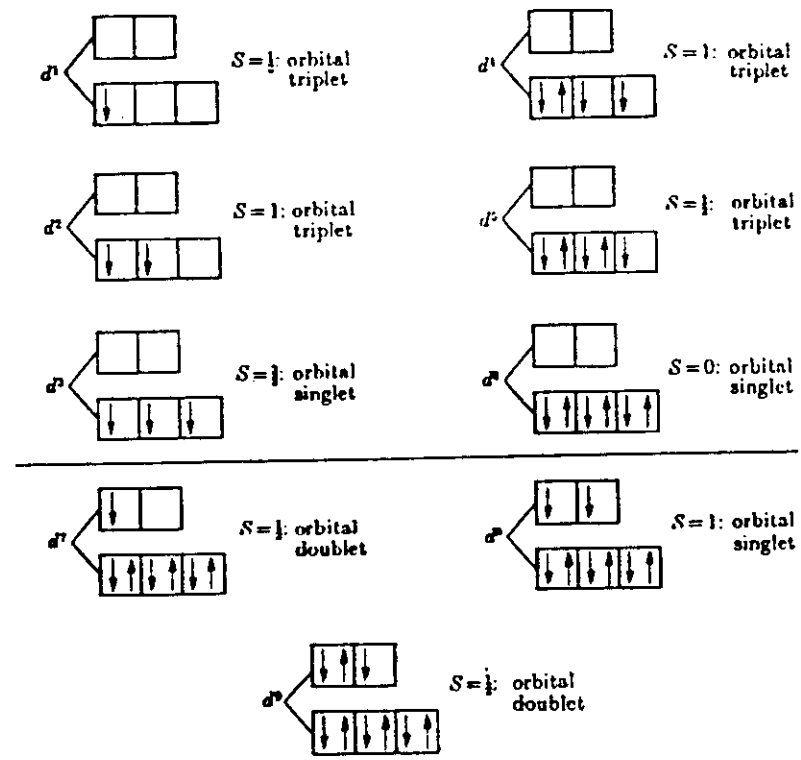

FIG. 7.8. Construction of the ground states of the d-configurations in an octahedral field using the strong crystal field approach, and assuming the crystal field energy to be larger than the spin coupling energy.

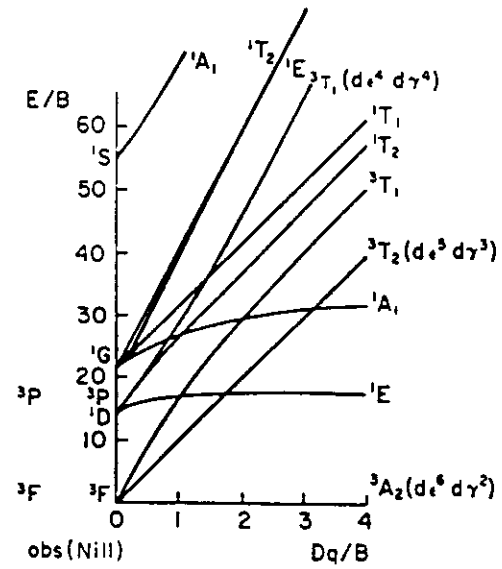

FIG. 5.2. The energy level diagram for the $N = 8$ system (Ni III : $3d^7(^4F)4s\,^5F \sim 51$; $\gamma = 4.71$; $B = 1030$).

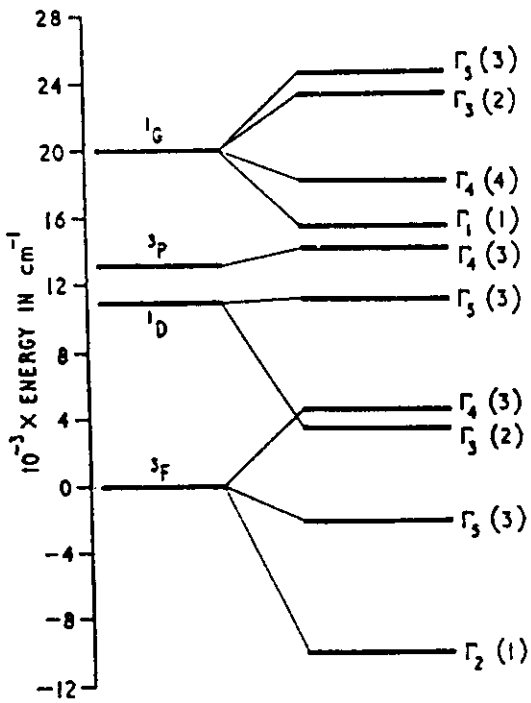

Fig. 2.12. Splittings of the ground and excited terms of $3d^8$ by an octahedral field. The magnitudes of the splittings are those appropriate for a Ni^{++} ion present as an "impurity" in a MgO host crystal (see Table 2.10). The labels for the states indicate the symmetries of the wavefunctions (Bethe's notation), the bracketed numbers indicating the orbital degeneracies remaining

$$V(\bar{r}_i) = - \sum_{j=1}^{N} \frac{Z_j \, e}{|\bar{R}_j - \bar{r}_i|}$$

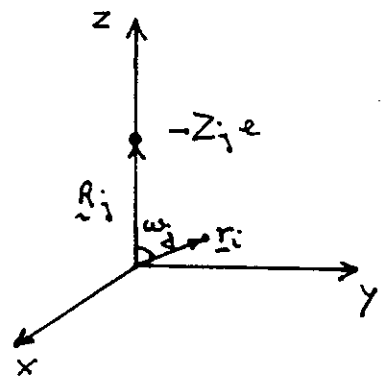

$r_i \ll R_j$

$$V(\bar{r}_i) = - e \sum_j Z_j \sum_{k=0}^{\infty} \frac{r_i^k}{R_j^{k+1}} P_k \, (\cos w_j)$$

$$P_k \, (\cos w_j) = \frac{4\pi}{2k+1} \sum_{q=-k}^{k} Y_k^q(\vartheta_i, \varphi_i) \; Y_k^{q\,*}(\vartheta_j, \varphi_j)$$

$$\mathcal{H}_{CF} = \sum_i \sum_{k=0}^{\infty} \sum_{q=-k}^{k} A'_{kq} \, r_i^k \, Y_k^q(\vartheta_i, \varphi_i)$$

$$A'_{kq} = e^2 \, \frac{4\pi}{2k+1} \sum_{j=1}^{N} \frac{Z_j \, Y_k^{q*}(\vartheta_j, \varphi_j)}{R_j^{k+1}} \, .$$

$$\mathcal{H}_{CF} = \sum_{k,q} A_{kq} \sum_{i=1}^{n} f_{kq}(x_i, y_i, z_i)$$

$$\downarrow$$

$$\mathcal{H}_{CF} = \sum_{k,q} A_{kq} \langle r^k \rangle \Theta_k \hat{O}_k^q$$

$$A_{kq} = \frac{2k+1}{4\pi} S_k^q A'_{kq}$$

$$\boxed{A_{kq} = S_k^0 \sqrt{\frac{2k+1}{4\pi}} \sum_{j=1}^{N} \frac{Z_j e^2}{R_j^{k+1}} K_{kq}(\theta_j, \varphi_j)}$$

$$B_{kq} = A_{kq} \langle r^k \rangle \Theta_k \times (1 - \sigma_k)$$

$$\boxed{\mathcal{H}_{CF} = \sum_{\substack{k=2 \\ (pari)}}^{2\ell} \sum_{q=-k}^{k} B_{kq} \hat{O}_k^q}$$

$$B_{kq} = \sum_{j=1}^{N} \overline{B}_k(R_j) K_{kq}(\theta_j, \varphi_j)$$

$$\mathcal{H}_{CF}^{cub} = B_4 (\hat{O}_4^0 + 5\hat{O}_4^4) + B_6 (\hat{O}_6^0 - 21 O_6^4)$$

S - state ions – EPR experiments

$3d^5$ Mn^{2+}, Fe^{3+} $\rightarrow$ $^6S_{5/2}$

$4f^7$ Eu^{2+}, Gd^{3+}, Tb^{4+} $\rightarrow$ $^8S_{7/2}$

Gd^{3+}

- line width sufficiently narrow till to RT
- hyperfine structure usually unresolved
- zero field splitting low enough to allow usually a detailed analysis of the transitions

$$|^8\mathcal{S}_{7/2}\rangle = s\,|^8S_{7/2}\rangle + p\,|^6P_{7/2}\rangle + d\,|^6D_{7/2}\rangle$$

+ smaller contributions

$s = 0.9866$

$p = 0.1618$

$d = -0.0123$

$$\psi^a_{0\sigma} = \alpha\, d^a_{x^2-y^2} + \xi\, d^a_{z^2} - \frac{\gamma}{\sqrt{2}}(-\sigma_x{}^2 + \sigma_x{}^4)$$
$$- \frac{\delta}{\sqrt{2}}(\sigma_y{}^5 - \sigma_y{}^3) - \sqrt{2}\,\varepsilon\,(-\sigma_z{}^6 + \sigma_z{}^1)$$

with

$$\sigma^i = n\,p^i \mp (1 - n^2)^{1/2}\,s^i\,,$$

$$g_x = 2.0023 - \frac{2\lambda_0\,\beta'^2}{\Delta yz}$$
$$\cdot[\alpha + \sqrt{3}\,\xi][\alpha + \sqrt{3}\,\xi - 2\alpha'\,S_{xy}]\,,$$
$$g_y = 2.0023 - \frac{2\lambda_0\,\beta^2}{\Delta xz}$$
$$\cdot[\alpha - \sqrt{3}\,\xi][\alpha - \sqrt{3}\,\xi - 2\alpha'\,S_{xy}]\,,$$
$$g_z = 2.0023 - \frac{8\lambda_0\,\beta_1{}^2}{\Delta xy}\,\alpha[\alpha - 2\alpha'\,S_{xy}]\,,$$

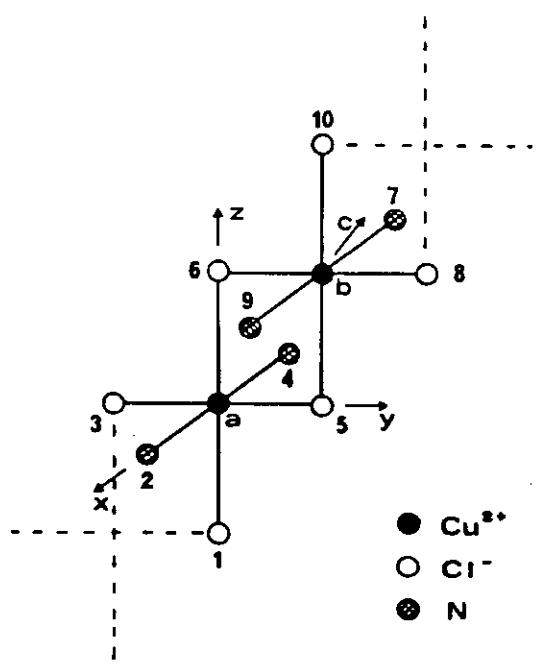

Fig. 1. A segment of a linear chain parallel to the c axis in CDP.

$CuCl_2 \cdot 2NC_5H_5$

G. Amoretti, V. Varacca and A. Vera - Z. Naturforsh. 34a, 353 (197
G. Amoretti, Z. Naturforsch. 33a, 130 (1978)
G. Amoretti and V. Varacca, J. Chem. Phys. 61 (74) 3651, 65 (76) 1511, 67 (77)

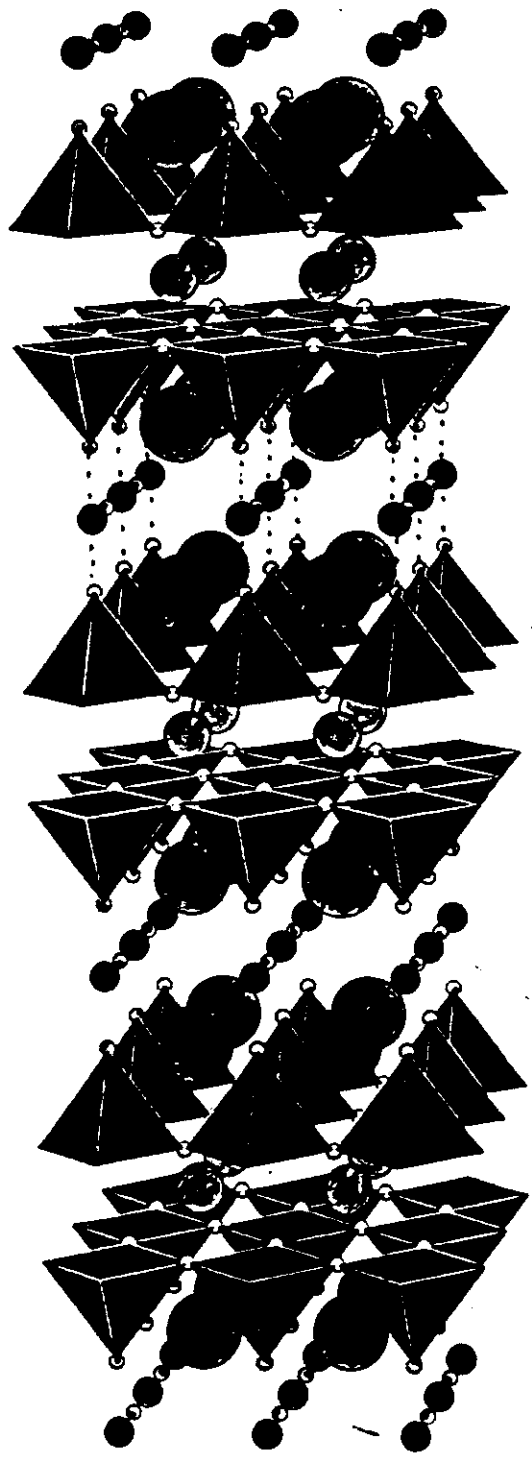

$YBa_2Cu_3O_7$

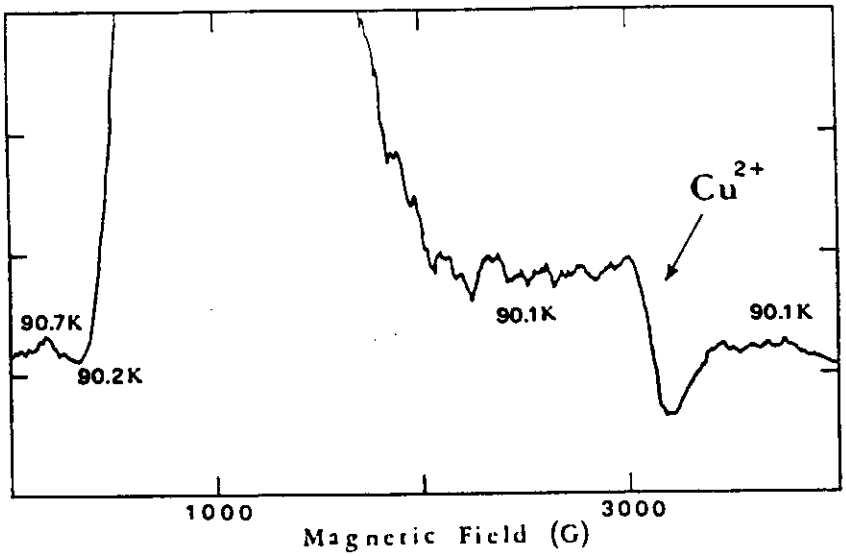

Fig. 1. The onset of the low-field intense non resonant absorption and the signal of localized Cu^{2+} ions. During the field sweep the temperature was slightly decreased across T_c. The superconductive transition is evidenced by the sudden rise of the signal at 90.2 K

which may be attributed to copper paramagnetic ions, as will be discussed later. The signals of samples I, were found to be about thirty times stronger in intensity after the sintered samples (~15 mg of material) were ground to the powder in an agate mortar. This fact can be explained in terms of complete penetration of the powder by the microwave field, taking into account that the skin depth is of the order of $10^{-2} - 10^{-3}$ cm for a sintered sample at 9 GHz. Sample II was ground to a powder too, for comparison with the other ones. The number of resonant spins has been determined by comparison with signals from known quantities of $CuSO_4 \cdot 5H_2O$. A maximum concentration of 5% of resonant copper ions has been observed in the type I samples showing the weakest Meissner effect (~15%). They will be called "Ia" in the following. The concentration is of the order of 1% for sample II and for the type I samples showing a stronger Meissner effect ($\gtrsim$40%, "Ib" samples).

The transition to the superconducting phase has been checked in the various samples by observing the onset temperature of the intense non-resonant low-field absorption (Fig. 1), and was found to be (90±0.5) K in all the cases.

The RT spectra for both the sintered and the powdered Ia compounds are shown in Fig. 2. Sample Ib and II give rise to very similar spectra. That of sample II is shown in Fig. 3. All these signals present the characteristics of powder spectra due to Cu^{2+} in the tetragonal symmetry. In the axial hypothesis, a reasonable decomposition allowed us to deduce the g values:

$g_{\parallel} = 2.21 \pm 0.02$

$g_{\perp} = 2.06 \pm 0.02$,

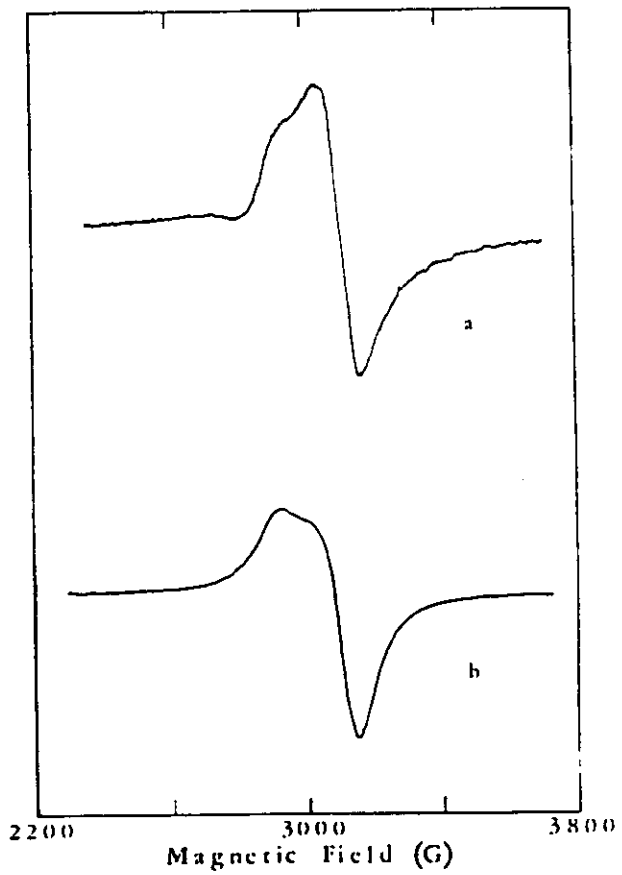

Fig. 2. RT spectra of Ia-type samples. a sintered, b powdered. The intensity is about thirty times greater in the second case

in line with those usually observed for copper in oxygen coordination, with $3d_{x^2-y^2}$ as the orbital ground state. These values, which are essentially constant

G. Amoretti, E. Buluggiu, A. Vera, G. Calestani and F.C. Matacotta, Z. Phys. B 72, 17 (1988)

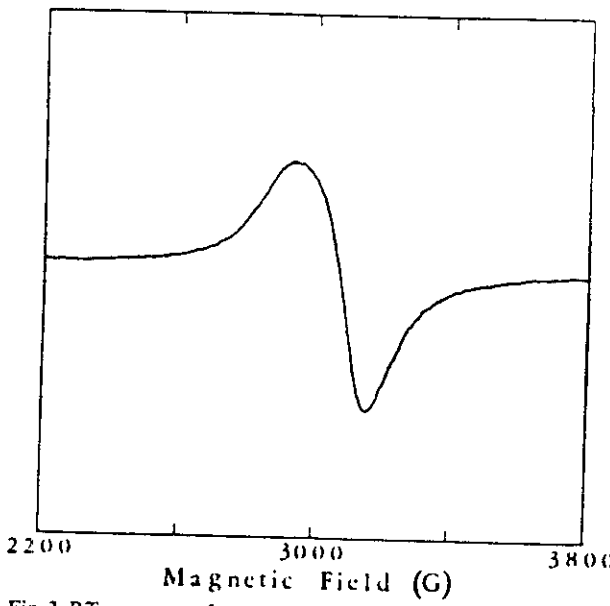

Fig. 3. RT spectrum of sample II (powdered)

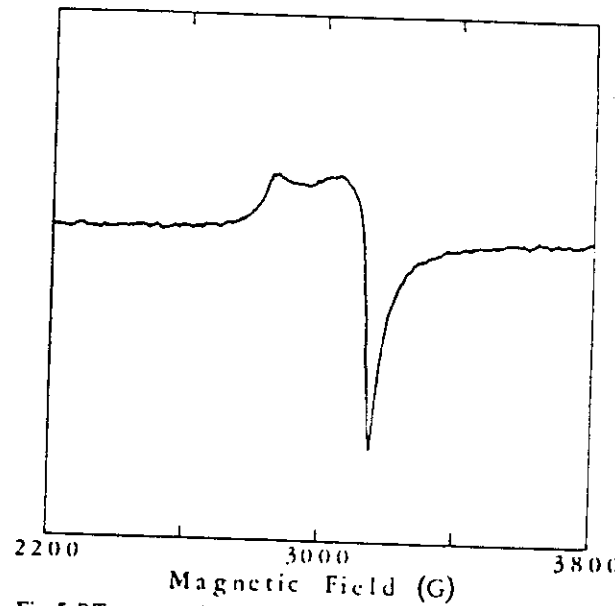

Fig. 5. RT spectrum frequently observed in the YBCO samples when damaged by hydration

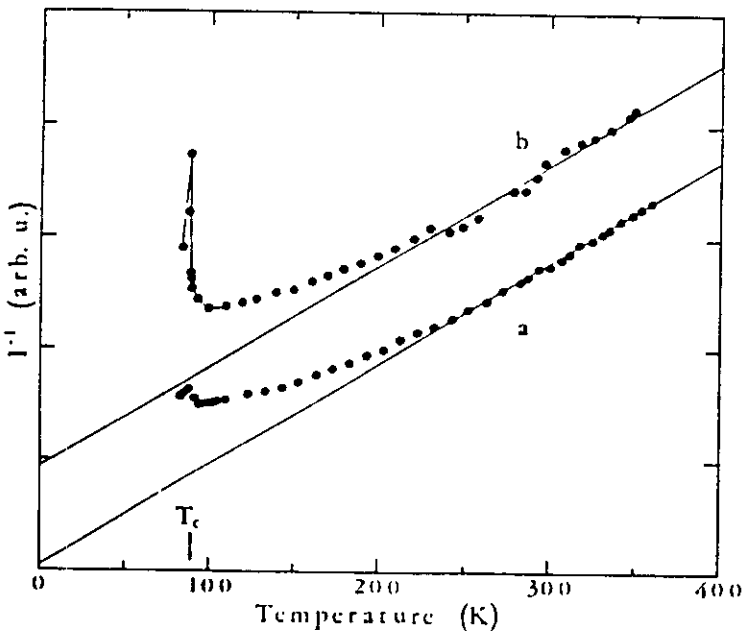

Fig. 4. Inverse peak-to-peak height (arbitrary units) of the ESR signal as a function of the temperature. a sample Ia. b sample Ib. The fitting of the high temperature tail is shown too

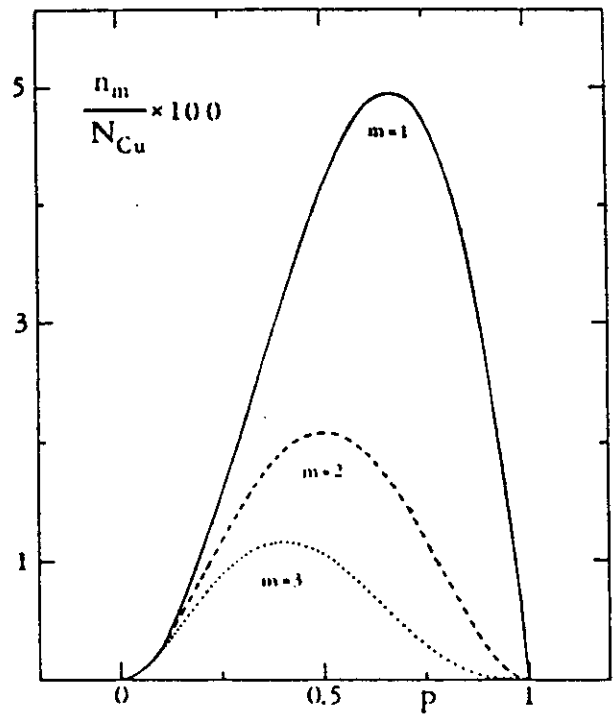

Fig. 6. The fraction of monomers, dimers and trimers in the linear chains versus p

Table 1. The values of n_m/N_{Cu} in percent, for some relevant values of p

m	p		
	1/3	1/2	2/3
1	2.5	4.2	4.9
2	1.6	2.1	1.6
3	1.1	1.0	0.5

$$n_m = \frac{N_{Cu}}{3}(1-p)^m p^2,$$

where N_{Cu} is the total number of copper atoms in the crystal and p is the fractional concentration of Cu^{3+} ions in the chains.

'Is there any other point to which you would wish to draw my attention?'
'To the curious incident of the dog in the night-time.'
'The dog did nothing in the night-time.'
'That was the curious incident.'
A. Conan Doyle in "Silver Blaze".

F. Mehran and P.W. Anderson
Solid State Commun. 71, 29 (1989)

$$\Delta\omega = \omega_A \frac{\xi}{a}$$

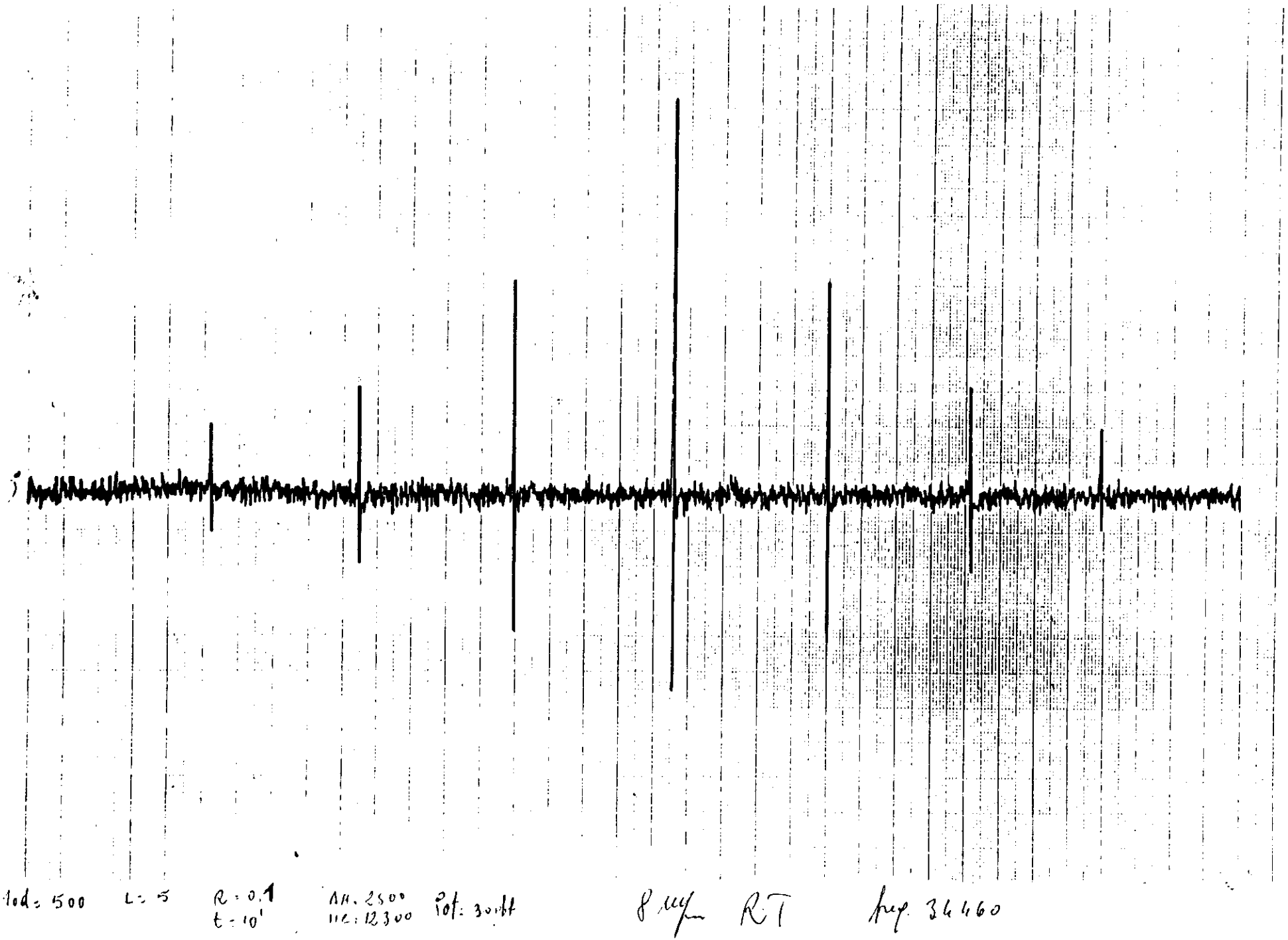

G. Amoretti, D.C. Giori, V. Varacca, J.C. Spirlet, J. Rebizant, Phys. Rev. B 20, 3573 (1979)

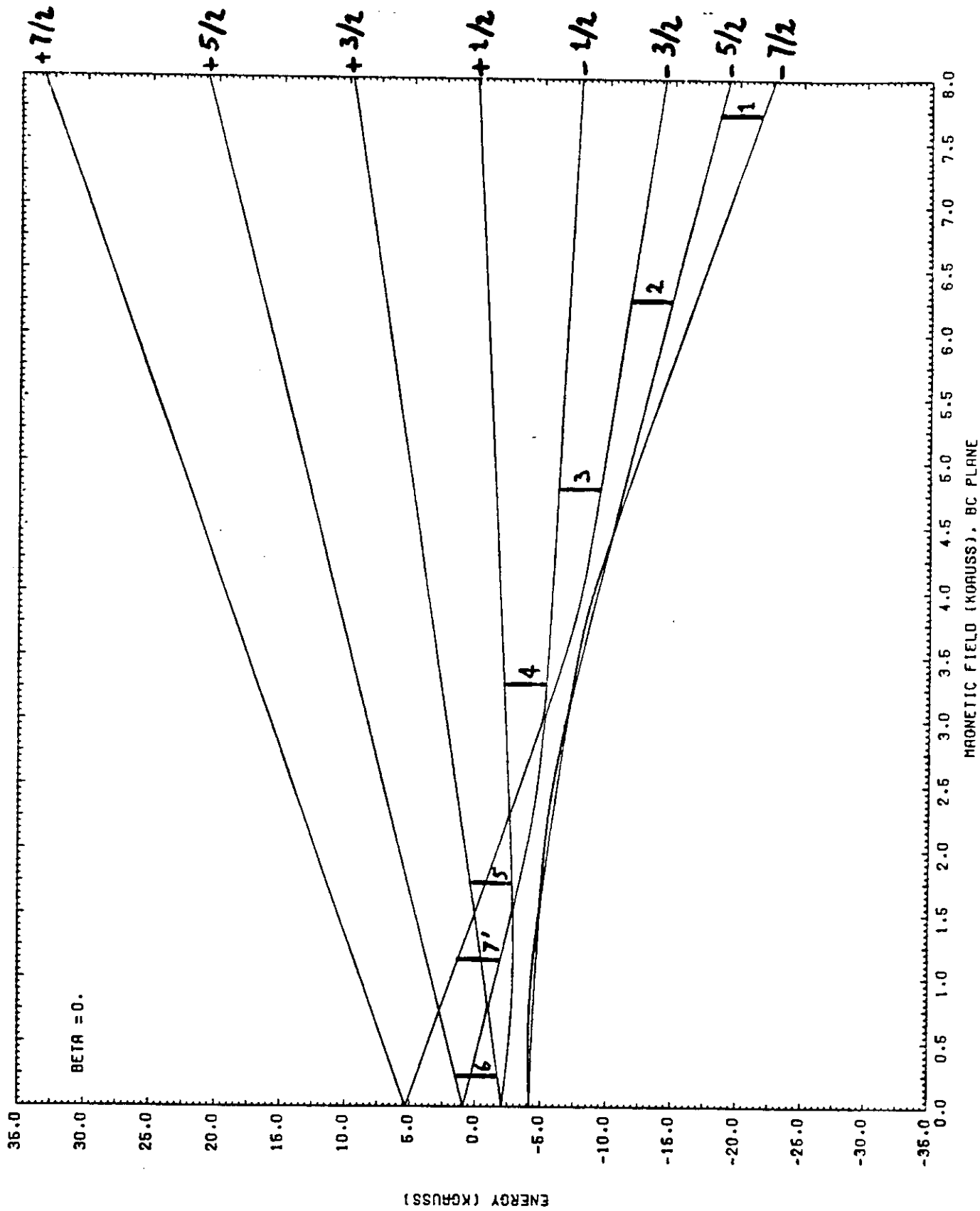
+7/2
+5/2
+3/2
+1/2
-1/2
-3/2
-5/2
-7/2
1
2
3
4
5
7'
6
BETA = 0.
ENERGY (KGAUSS)
MAGNETIC FIELD (KGAUSS), BC PLANE
35.0
30.0
25.0
20.0
15.0
10.0
5.0
0.0
-5.0
-10.0
-15.0
-20.0
-25.0
-30.0
-35.0
0.0
0.5
1.0
1.5
2.0
2.5
3.0
3.5
4.0
4.5
5.0
5.5
6.0
6.5
7.0
7.5
8.0

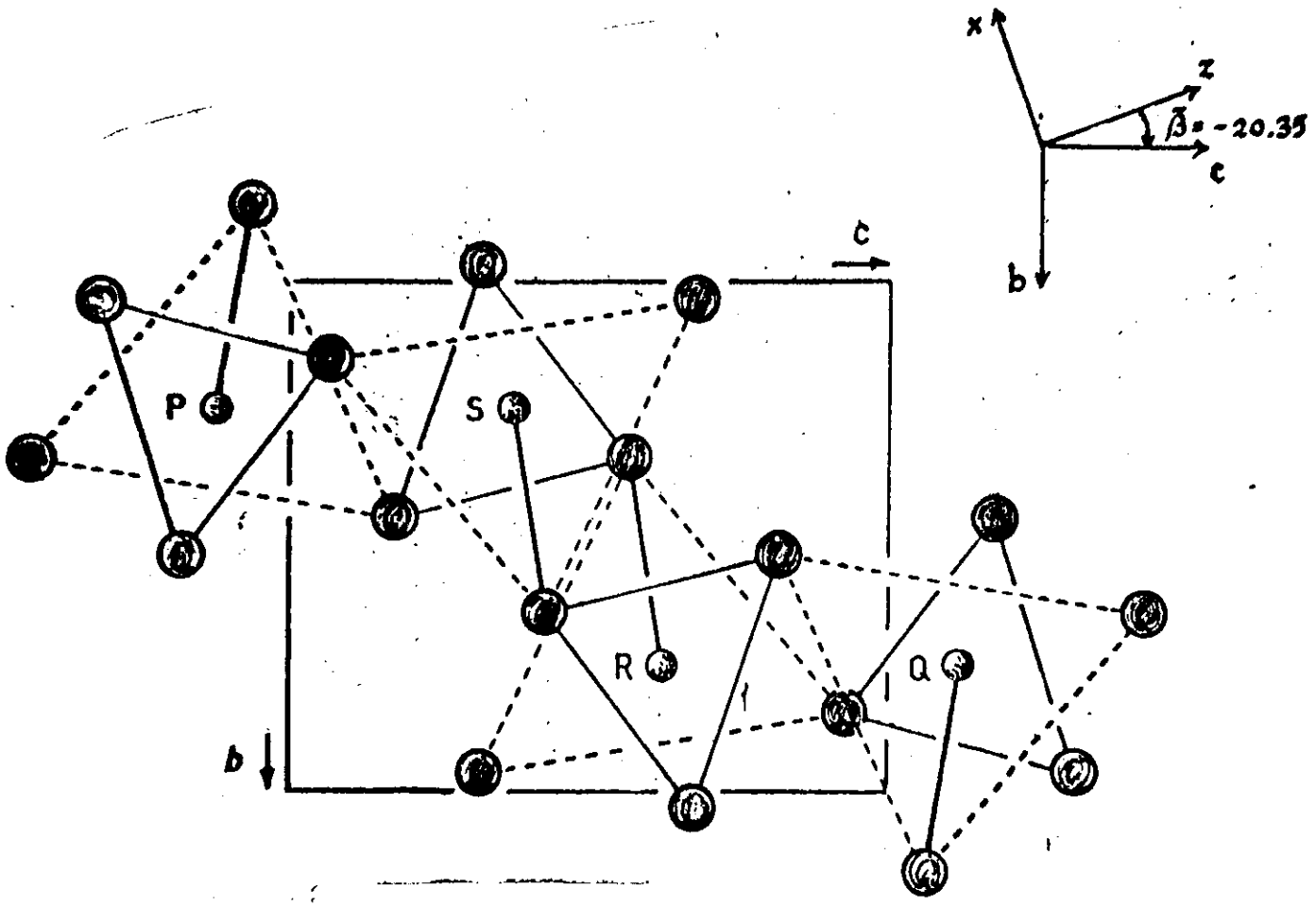

$ThS_2 : Gd^{3+}$

a = 4.259 Å

b = 7.249 "

c = 8.600 "

ThS_2

* Gd^{3+} sostituzionale

** Gruppo puntuale C_s

	R	K_2^0	K_2^1	K_2^2
S_1	2.74	0.989	-0.521	0.011
S_2	2.80	0.128	0.142	-0.868
S_3	2.94	-0.126	2.595	1.126
S_4	3.00	-0.270	1.369	-0.231
S_5	3.05	0.092	-2.933	0.908
S_6	3.13	-0.337	-1.293	-0.054

Fig. 1

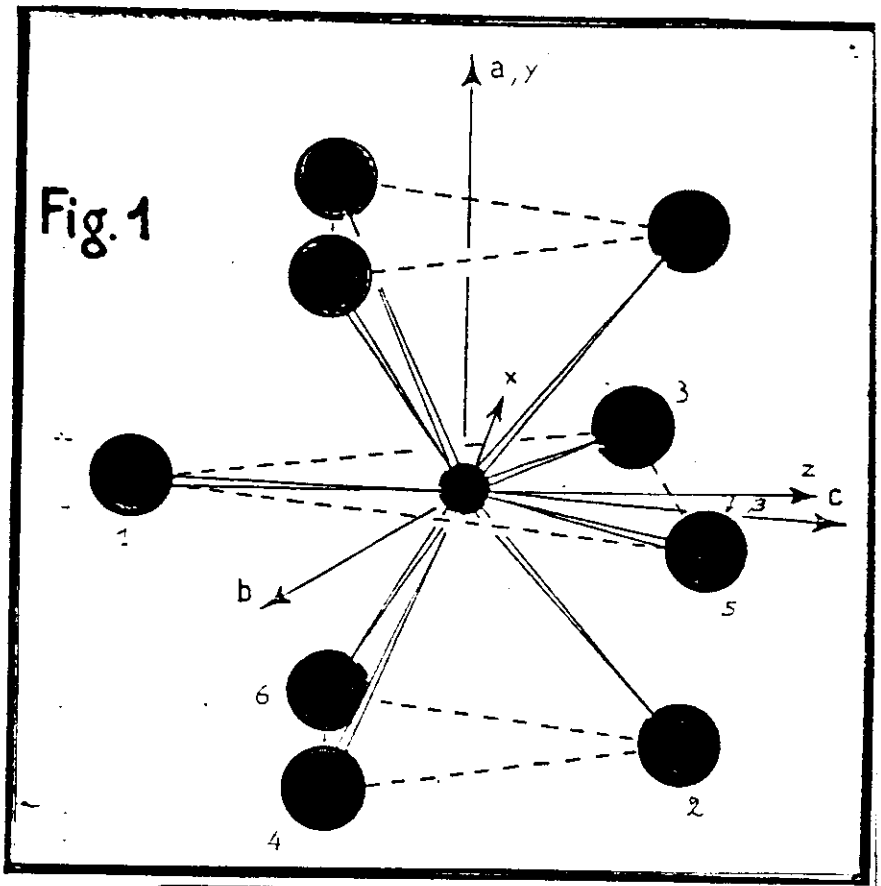

n \ m	0	1	2	3	4
2	708	0	-243	-	-
4	-4.0	25	-4.0	-125	-20

ThOS

* Gd^{3+} sostituzionale

** Gruppo puntuale C_{4v}

	R	K_2^0
O	2.39	-0.025
S	2.98	-0.321
S'	3.01	1.

n \ m	0	4
2	183.33	-
4	-1.704	-28.3

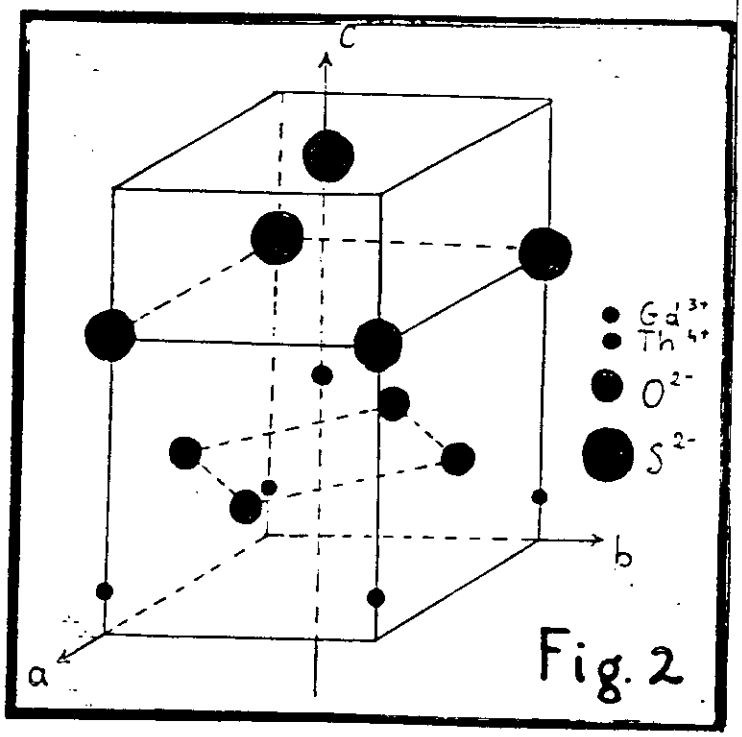

Fig. 2

Fig. 4

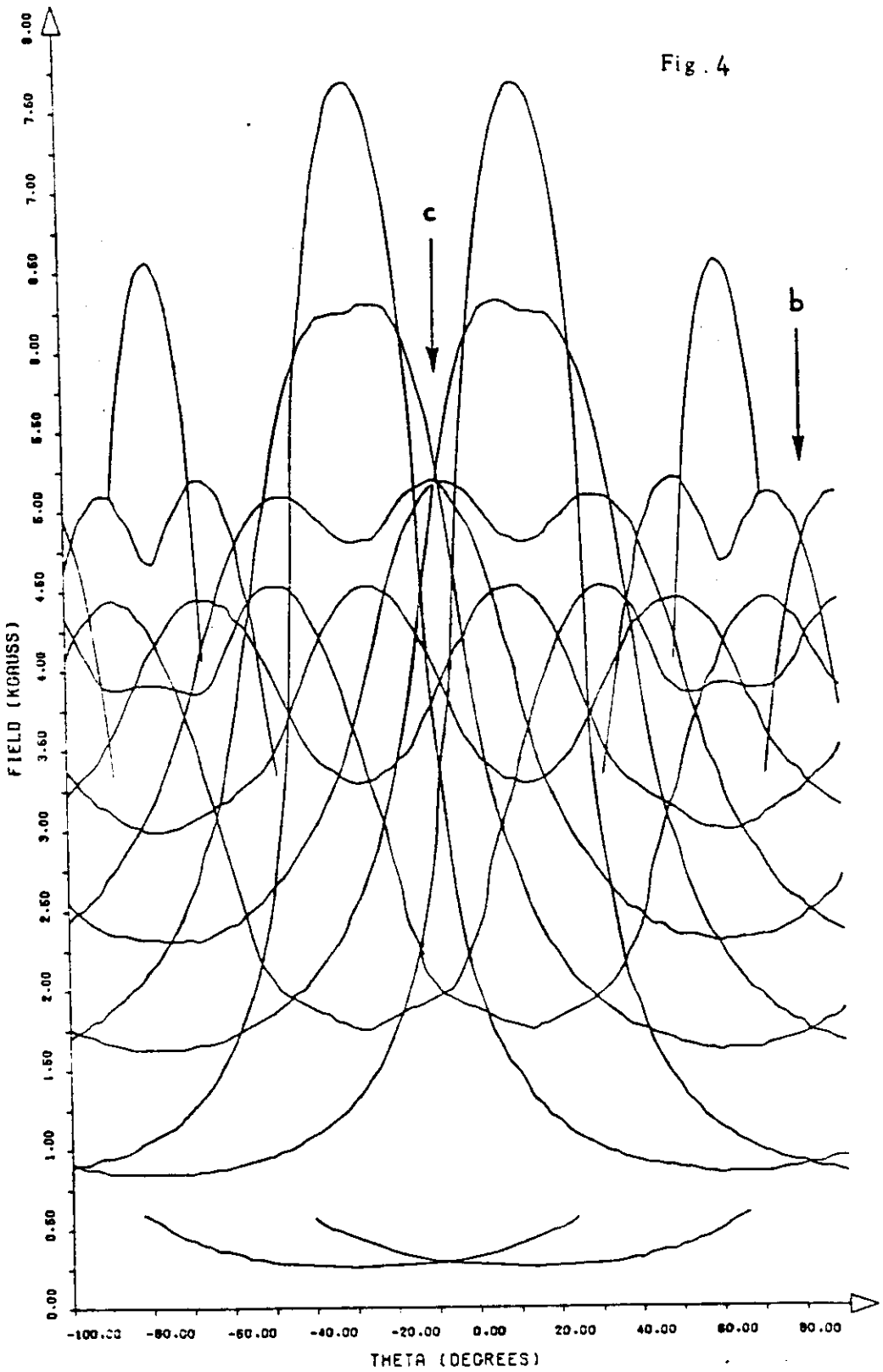

$ThS_2 : Gd^{3+}$

G. Amoretti, D.C. Giori and V. Varacca, Z. Naturforsh. 36a, 111

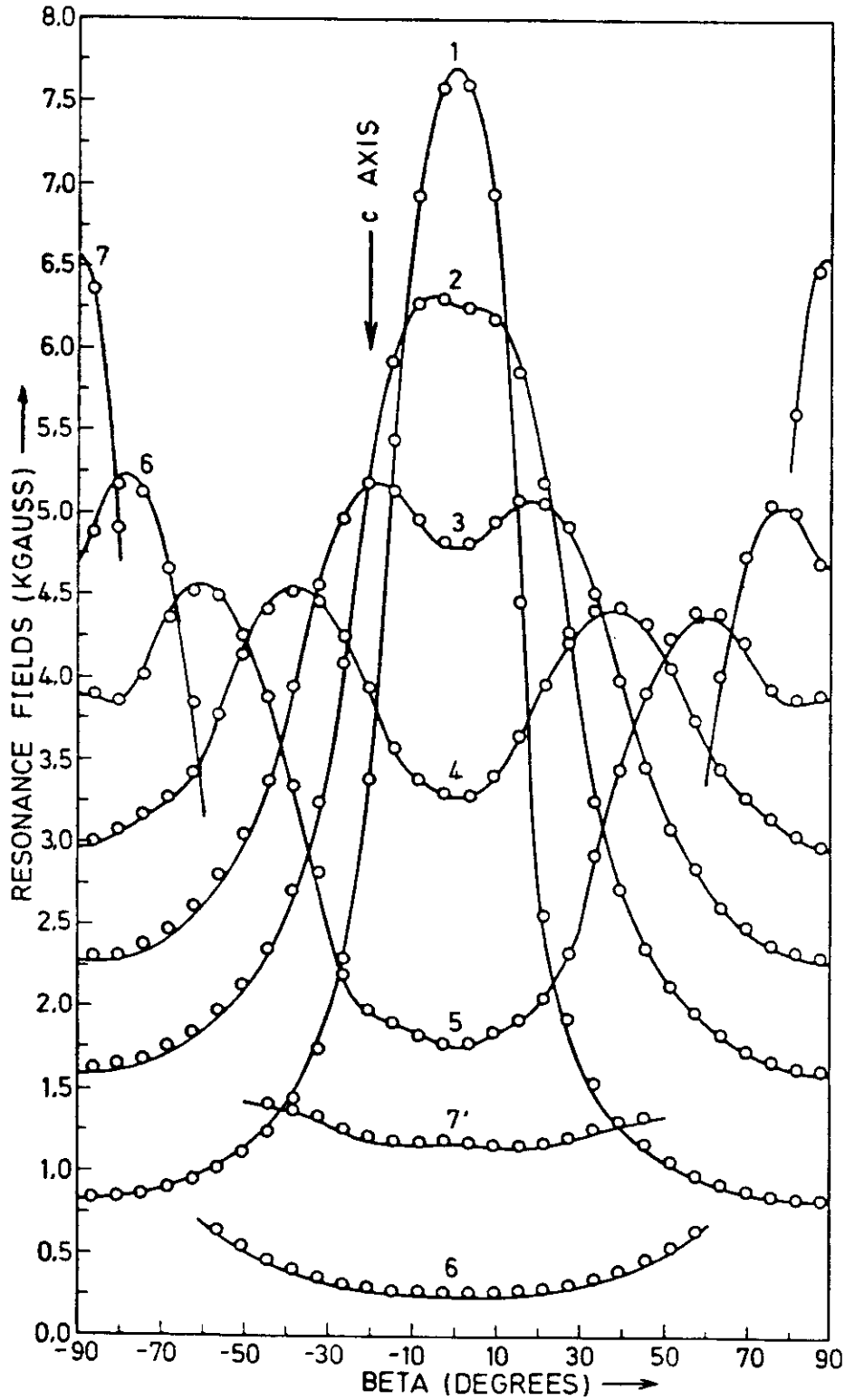

$Th\,S_2 : Gd^{3+}$

Fig. 5

G. Amoretti, D.C. Giori and V. Varacca, Z. Naturforsch. 36a, 1163 (1981)

« Application of the superposition model to the analysis of crystal field parameters in low symmetry systems : the use of a two exponents power law »

The SPM assumes that the total crystal field on a given ion can be constructed from a sum of axially symmetric contributions of the ligands [1].

This assumption is consistent with the hypothesis that :

- the coordinated ions make the dominant contribution to the crystal field
- this contribution is due principally to overlap and covalency effects.

If the CF hamiltonian is written as

$$\mathcal{H}_{CF} = \sum_{n,m} B_n^m O_n^m \qquad (1)$$

with

$$B_n^m = A_n^m \langle r^n \rangle \Theta_n \qquad (2)$$

(Θ_n: Stevens coefficients)

the SPM model assumes that

$$A_n^m \langle r^n \rangle = \sum_{i \text{ (ligands)}} \bar{A}_n(R_i)\, K_n^m(\theta_i, \varphi_i) \qquad (3)$$

($\bar{A}_n(R_i)$: intrinsic parameter; $K_n^m(\theta_i, \varphi_i)$: coordination factors)

or equivalently

$$B_n^m = \sum_i \bar{B}_n(R_i)\, K_n^m(\theta_i, \varphi_i) \qquad (4)$$

with

$$\bar{B}_n(R_i) = \bar{A}_n(R_i)\, \Theta_n \quad . \qquad (5)$$

The point charge approximation corresponds to

$$\bar{A}_n(R_i) = S_n^\circ \sqrt{\frac{2n+1}{4\pi}}\, \frac{e^2 z_i \langle r^n \rangle}{R_i^{n+1}} \qquad (6)$$

where

$$S_2^\circ = \sqrt{\pi/5} \quad , \quad S_4^\circ = \sqrt{\pi}/12 \quad , \quad S_6^\circ = \tfrac{1}{8}\sqrt{\pi/13} \qquad (6')$$

and the effective charge z_i is positive for negative ions.

G. Amoretti, G. Calestani and D.C. Giori, Z. Naturforsh. 39a (1984) 778

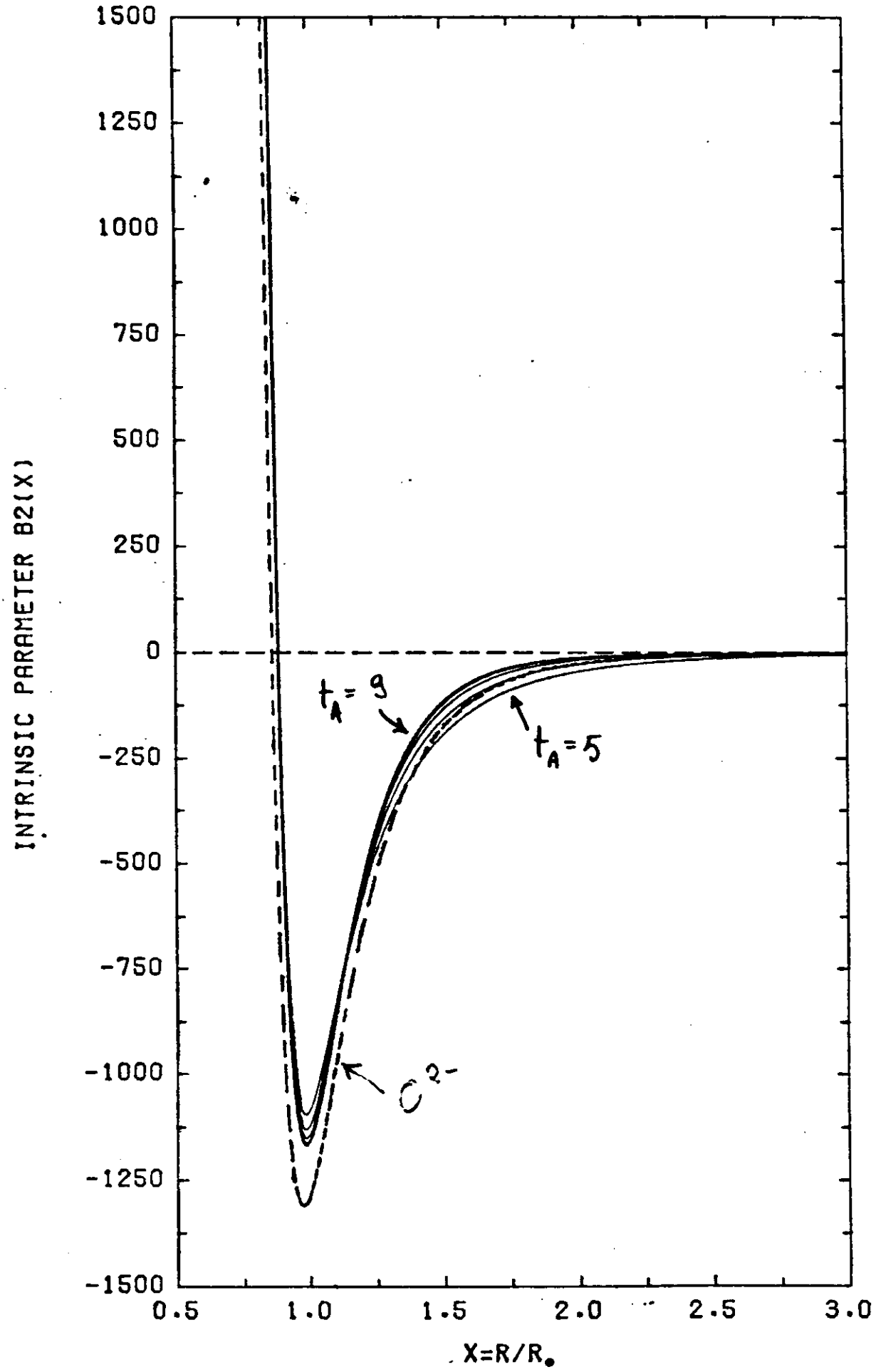

Paramagnetic resonance and local position of Cr^{3+} in ferroelectric $BaTiO_3$

K. A. Müller and W. Berlinger
IBM Zurich Research Laboratory, 8803 Rüschlikon, Switzerland

J. Albers
Physics Department, Universität des Saarlandes, 6600 Saarbrücken, West Germany

(Received 6 June 1985)

EPR spectra of Cr^{3+}, $S=\frac{3}{2}$, substituting for Ti^{4+} are reported as a function of temperature T in all four phases of $BaTiO_3$. In the three ferroelectric phases (FEP's), the principal axis of the Hamiltonian is always along the polar axis. There are two crystal-field terms, one proportional to the square of the polarization and a large one linear in T. The latter is the *same* in all FEP's. The existence of the first term shows that the Cr^{3+} remains centered in the octahedral cell. The existence of the latter, not observed for Fe^{3+}, points to large thermal fluctuations of the Cr^{3+}. These are ascribed to the absence of antibonding, repelling e_g electrons directed towards the oxygen atoms which are present for Fe^{3+}. Saturation of the $b_2^0(T)$ term for low T is accounted for by a Debye model for Cr^{3+} with an energy of only 236.6 K, proving independently a flat ionic potential for Cr^{3+}. The picture of considerable Cr^{3+} amplitude fluctuations agrees with an effectively reduced Cr^{3+}-O^{2-} distance of 0.02 Å compared to the Fe^{3+}-O^{2-} distance obtained from the superposition-model analysis. The latter yields the correct sign and magnitude of the crystal-field b_2^0 terms in all FEP's. It confirms that a maximum of the intrinsic superposition-model parameter $\bar{b}_2(R)$ for Cr^{3+}, derived earlier by Müller and Berlinger, occurs for R between 1.95 and 1.96 Å.

I. INTRODUCTION

Recently, Siegel and Müller[1] were able to interpret some two-decade-old paramagnetic resonance experiments on Fe^{3+} substituting for Ti^{4+} in $BaTiO_3$. These early experiments of Hornig, Rempel, and Weaver[2] were carried out as a function of temperature in the cubic and tetragonal ferroelectric phases (FEP's). Studies of Sakudo and Unoki[3] extended the investigations to the orthorhombic and rhombohedral phases for one specific temperature in each of the two phases. It was shown in the aforementioned analysis, using the superposition model with parameters determined earlier,[4] that the Fe^{3+} participates by less than an order of magnitude in the collective motion of the Ti^{4+} ions responsible for ferroelectricity, i.e., the Fe^{3+} remains at the center of the oxygen octahedron in all three ferroelectric phases.

The sizes of Ti^{4+} and Fe^{3+} in octahedral oxygen coordination are nearly the same. The difference in behavior, that one undergoes a cooperative transition and the other remains centered, can have two origins. (a) The Ti^{4+} has an empty $3d$ shell, whereas that of the Fe^{3+} is half-filled. It has been discussed that the emptiness of the Ti^{4+} d shell is crucial for the occurrence of the ferroelectricity.[1] (b) There is a charge difference of one unit between Ti^{4+} and Fe^{3+}. In a recent theoretical study, Sangster[5] showed the occurrence of radial enhancement of ions owing to the charge misfit between the substituted ion and the impurity. Thus the radius of Fe^{3+} is enhanced in $BaTiO_3$ as compared to that in an oxide, where it replaces an intrinsic trivalent ion. In order to elucidate further the two possible reasons for the centering of the Fe^{3+} just mentioned, another trivalent ion with nearly the same ionic radius as that of Fe^{3+},[6] but with a different $3d$ configuration, has been studied.

Cr^{3+} is such an ion, but with an electron configuration $3d^3$ as compared to Fe^{3+} with $3d^5$. Whereas Fe^{3+} in the high-spin configuration has its two subshells with t_{2g} and e_g character half-filled, $(t_{2g})^3,(e_g)^2$, Cr^{3+} has only the t_{2g} subshell half filled with configuration $(t_{2g})^3$ and the (e_g) shell empty. The $(e_g)^2$ are antibonding σ orbitals and will cause a larger repulsion from the negative oxygen shells to keep the Fe^{3+} centered; see Fig. 1. On the other hand, the $(t_{2g})^3$ are essentially nonbonding, having their charge density pointing midway between the oxygen electron density. Recent uniaxial stress experiments on Cr^{3+} in cubic MgO at room temperature indicated that Cr^{3+} may be slightly off center along the $\langle 100\rangle$ cubic positions.[7] Thus Cr^{3+} appeared as a valid candidate to decide whether the $3d^n$ configuration or the size enhancement, owing to the charge misfit, is more important.

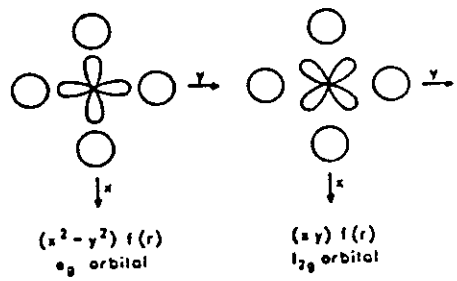

FIG. 1. Shapes of e_g and t_{2g} orbitals in octahedral coordination.

EPR of Gd^{3+} in a Single Crystal of Thorium disulfide (ThS_2)

G. Amoretti, D. C. Giori, and V. Varacca

Gruppo Nazionale di Struttura della Materia del Consiglio Nazionale delle Ricerche and Istituto di Fisica dell'Università, Parma, Italy

Z. Naturforsch. 36a, 1163–1168 (1981); received September 7, 1981

In this paper we report the experimental angular behaviour of the EPR spectra for a single crystal of Thorium disulfide (ThS_2) doped with Gd^{3+} at very low concentration (of the order of 10 p. p. m.). The experimental data are interpreted in terms of a spin Hamiltonian which reflects the crystal field symmetry at the Th site, that is monoclinic C_s, and therefore shows that the doping ions enter substitutionally without lowering the site symmetry. The low symmetry and the unusually large values of the crystal field parameters b_2^0 and b_2^2 have made it necessary to use a numerical fitting procedure, starting from the exact numerical diagonalization of the energy matrix for any given direction of the static magnetic field.

Superposition Model Analysis of the Spin Hamiltonian Parameters of Two Gd^{3+} Doped Thorium Dichalcogenides

G. Amoretti *, C. Fava, and V. Varacca *

Istituto di Fisica dell'Università, Parma, Italy

Z. Naturforsch. 37a, 536–545 (1982); received January 8, 1982

The spin Hamiltonian parameters of Gd^{3+} in a single crystal of Thorium disulfide (ThS_2) are analysed by means of the superposition model, in its most general form of a two exponents power law. In fact, the approximated one exponent power law is not suitable for this compound, where the ion-ligand distances show a quite large spread. The results of the analysis are then applied to the case of Gd^{3+} doped Thorium oxysulfide (ThOS), where the fitting of the experimental data is possible only assuming some distortion of the ligand cage.

The Refined Structure of ThS_2 and the Implications on the Superposition Model Analysis of ThS_2: Gd^{3+} Spin Hamiltonian Parameters

G. Amoretti *, G. Calestani **, and D. C. Giori *

University of Parma, Italy

Z. Naturforsch. 39 a, 778–782 (1984); received May 21, 1984

The crystal structure of ThS_2 has been refined starting from single crystal diffractometry data. The accurate determination of the positional parameters allows us to reexamine the SPM analysis of the second degree crystal field parameters for Gd^{3+} in ThS_2 matrix. The fitting of the EPR data is still possible by means of a suitable two exponents power law for the intrinsic parameter only if the substitutional Gd^{3+} ion displaces in the mirror (bc) plane with respect to the undistorted Th^{4+} site. The resulting increase of the mean metal-ligand distances agrees with the expected expansion of the ligand cage around the trivalent Gd ion. The applicability of the proposed method to examine the impurity induced distortions in an host crystal is discussed too.

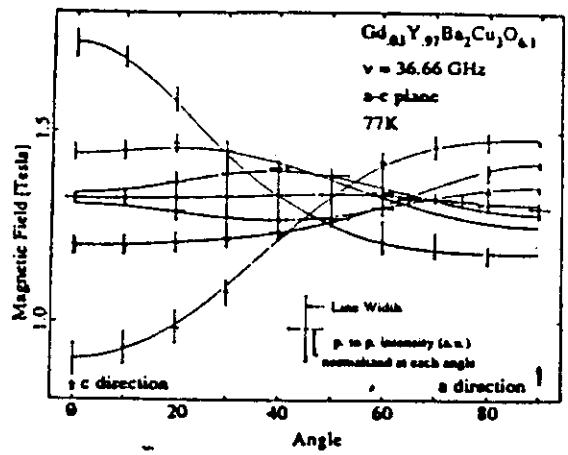

Fig. 1. Angular dependence of Gd ESR at K_a-band in $YBa_2Cu_3O_{6+}$ in the a–c plane at 77 K. Note that the lines in each measurements are not error bars but line width (vertical line) and peak to peak intensity (horizontal line). Intensities which are too small to be indicated are represented by a small circle. The intensities are normalized separately for each angle.

Table I
Crystal field parameters in MHz and g-value of Gd in $YBa_2Cu_3O_{6+z}$ at ~35 GHz and 77 K. The $T_c \sim 70$ K for the $x=0.7$ material.

x	$3B_2^0 = D$	B_4^0	B_4^4	g-value
0.1 ± 0.1	1307 ± 5	3.01 ± 0.1	−11.4 ± 0.2	1.989 ± 0.005
0.7 ± 0.1	1359 ± 15	0.75 ± 0.2	−9.03 ± 0.5	1.996 ± 0.005

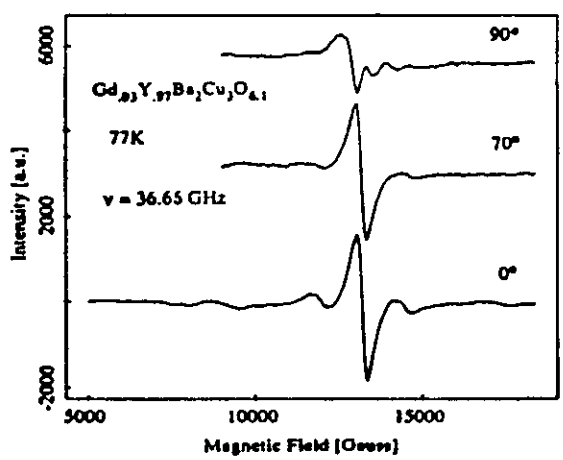

Fig. 2. The spectra corresponding to fig. 1 for $H=0$, 70 and 90 degrees.

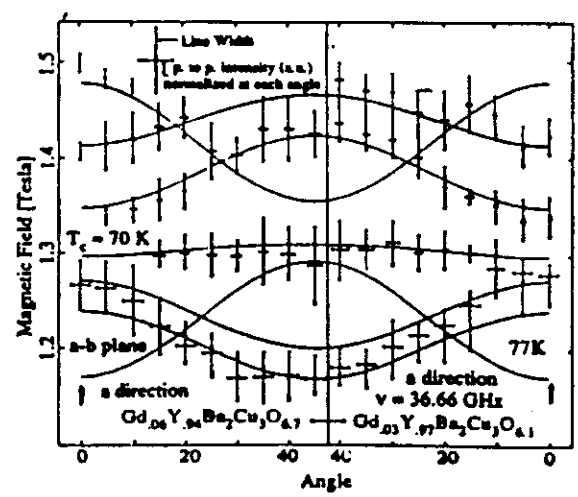

Fig. 3. Angular dependence of Gd ESR at K_a-band for $YBa_2Cu_3O_{6.7}$ and $YBa_2Cu_3O_{6.1}$ and taken in the a–b plane at 77 K. Note that, again, the lines in each measurements are not error bars but line width (vertical line) and peak to peak intensity (horizontal line), and that the intensities are normalized separately for each angle.

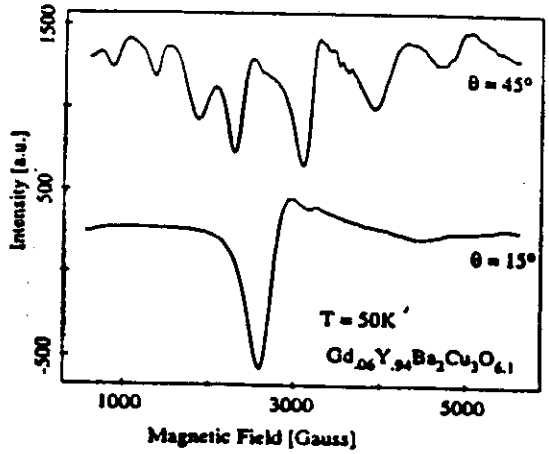

Fig. 4. The spectra at X-band for $\theta = 15°$ and $\theta = 45°$ away from the a direction in the a–b plane for $Gd_{0.06}Y_{0.94}Ba_2Cu_3O_{6.1}$.

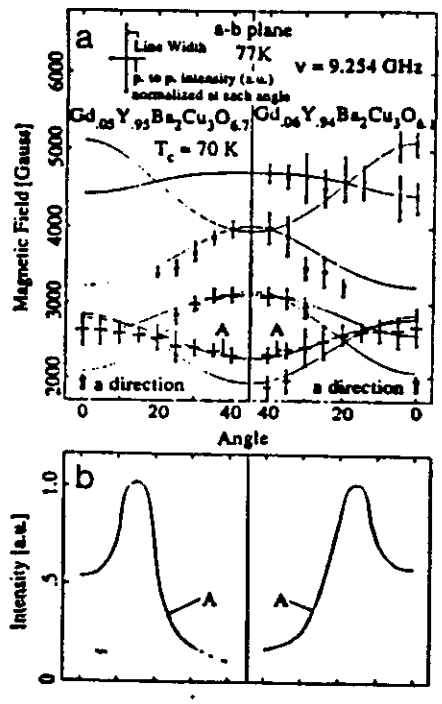

Fig. 5 (a) Angular dependence of Gd ESR at X-band for $YBa_2Cu_3O_{6.1}$ and $YBa_2Cu_3O_{6.7}$ at 77 K. Note that significance of the horizontal and vertical lines is as for figs. 1 and 3. (b) Peak to peak intensities of line A for different directions.

D. Shaltiel et al. (1989)

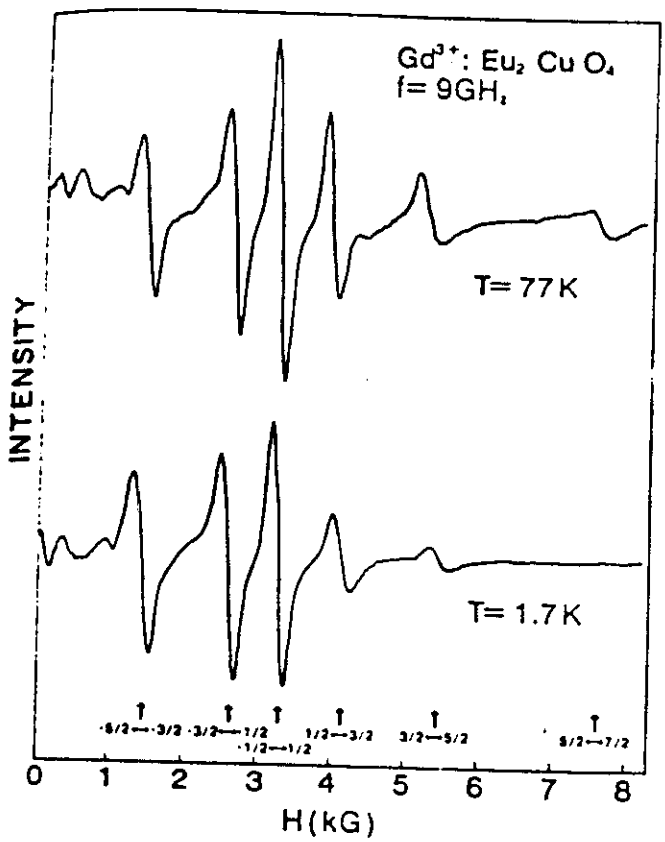

FIG. 1. ESR spectra of Eu_2CuO_4 doped with 1.5 at.% Gd, taken at 9 GHz with the external magnetic field parallel to the c axis. Notice the reduced intensity of the high-field fine-structure lines at 1.7 K. Also, notice that due to the large crystal-field splitting, the $-\frac{7}{2} \leftrightarrow -\frac{5}{2}$ transition cannot be observed at this frequency.

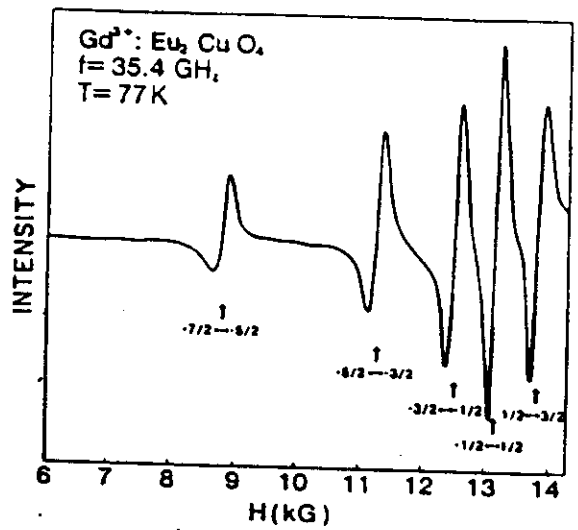

FIG. 2. ESR spectrum of Eu_2CuO_4 doped with 1.5 at.% Gd, taken at 35 GHz with the magnetic field parallel to the c axis. Notice that at this frequency we do observe the low-field $-\frac{7}{2} \leftrightarrow -\frac{5}{2}$ fine-structure line.

TABLE I. Crystal-field parameters and g_1 values for dilute Gd^{3+} ions in Eu_2CuO_4.

Temperature (K)	b_2^0 (10^{-4} cm^{-1})	b_4^0 (10^{-4} cm^{-1})	g_1	Frequency (GHz)
5	−486(7)	−32(2)	1.82(1)	9.25
30	−492(7)	−32(2)	1.84(1)	9.25
84	−509(7)	−37(2)	1.90(1)	9.25
77	−502(7)	−37(2)	1.91(1)	9.00
77	−524(10)	−40(2)	1.94(1)	35.4
Room temperature	−505(10)	−40(2)	1.95(1)	35.4

Rao, Tovar, Oseroff, Vier, Shultz, Thompson, Cheong and Fisk
Phys. Rev. B 38 (1988) 8920

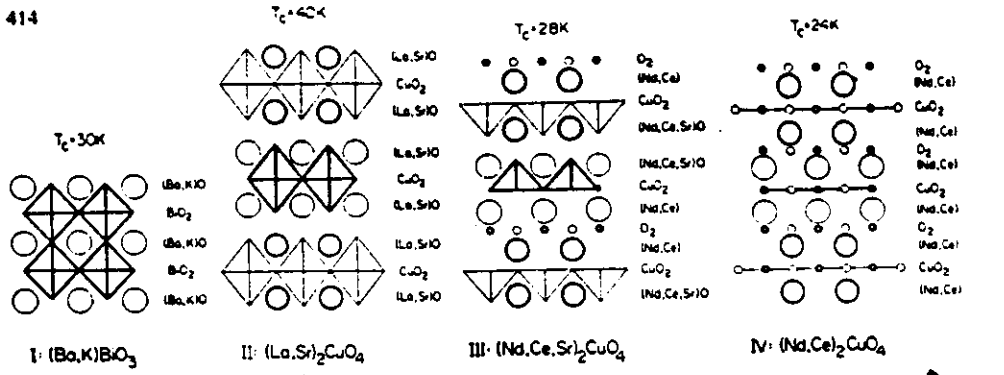

I: $(Ba,K)BiO_3$ II: $(La,Sr)_2CuO_4$ III: $(Nd,Ce,Sr)_2CuO_4$ IV: $(Nd,Ce)_2CuO_4$ a

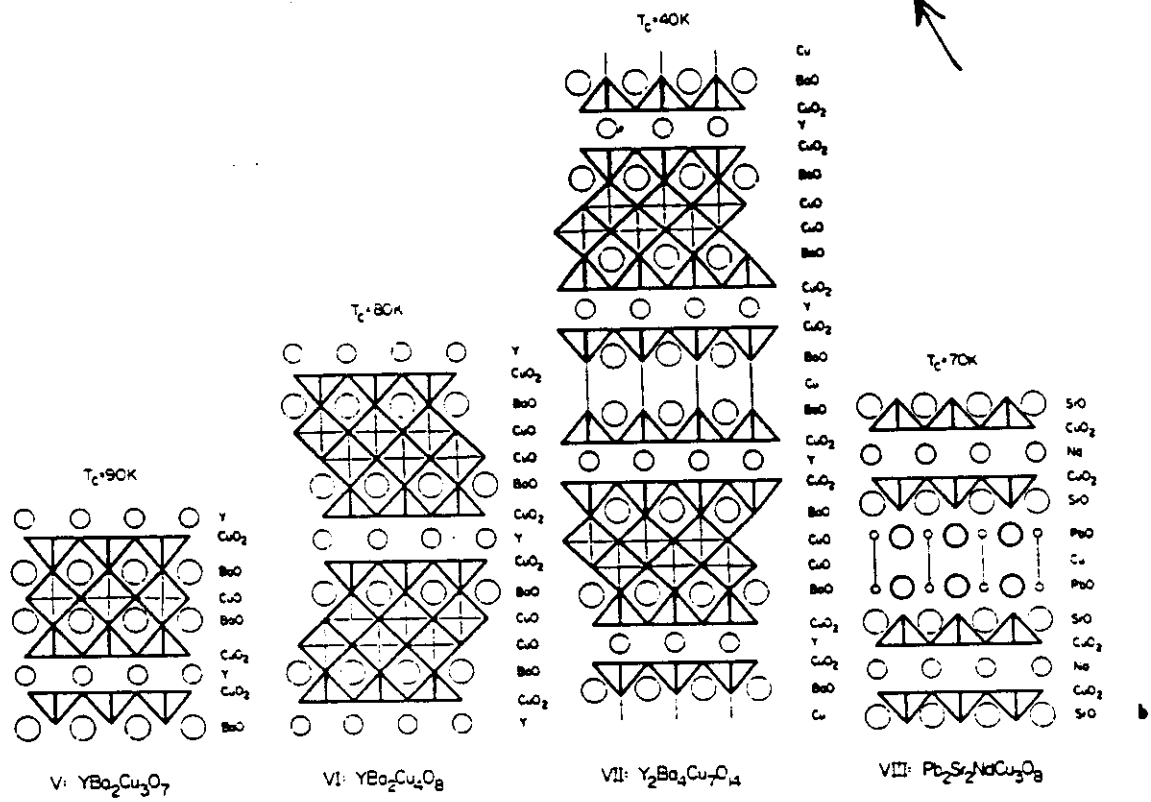

V: $YBa_2Cu_3O_7$ VI: $YBa_2Cu_4O_8$ VII: $Y_2Ba_4Cu_7O_{14}$ VIII: $Pb_2Sr_2NdCu_3O_8$ b

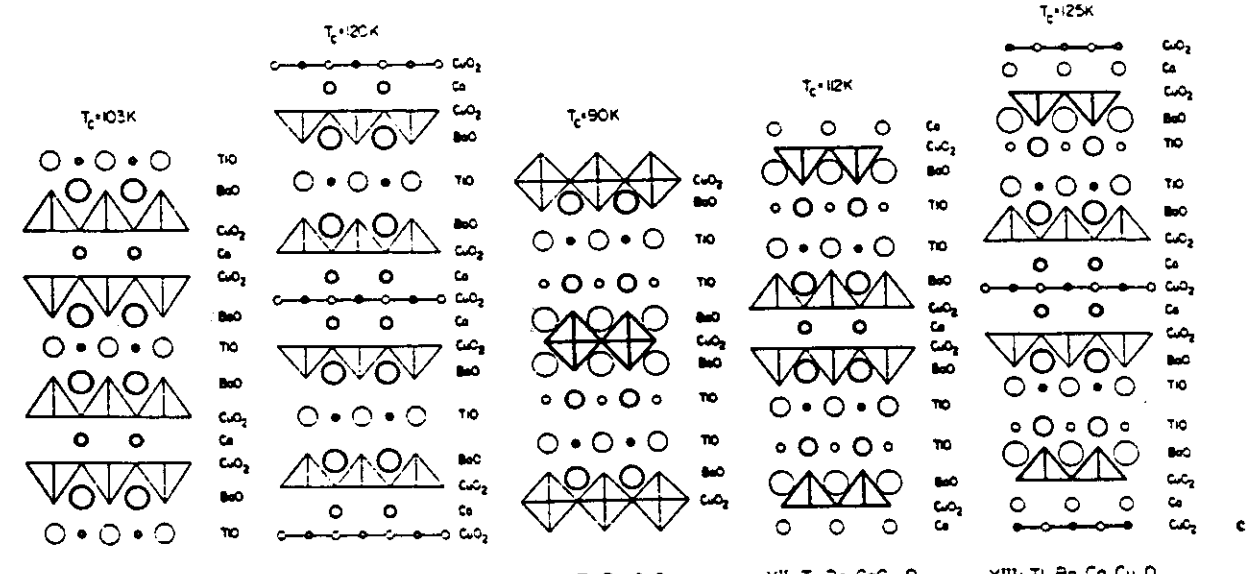

IX: $TlBa_2CaCu_2O_7$ X: $TlBa_2Ca_2Cu_3O_9$ XI: $Tl_2Ba_2CuO_6$ XII: $Tl_2Ba_2CaCu_2O_8$ XIII: $Tl_2Ba_2Ca_2Cu_3O_{10}$ c

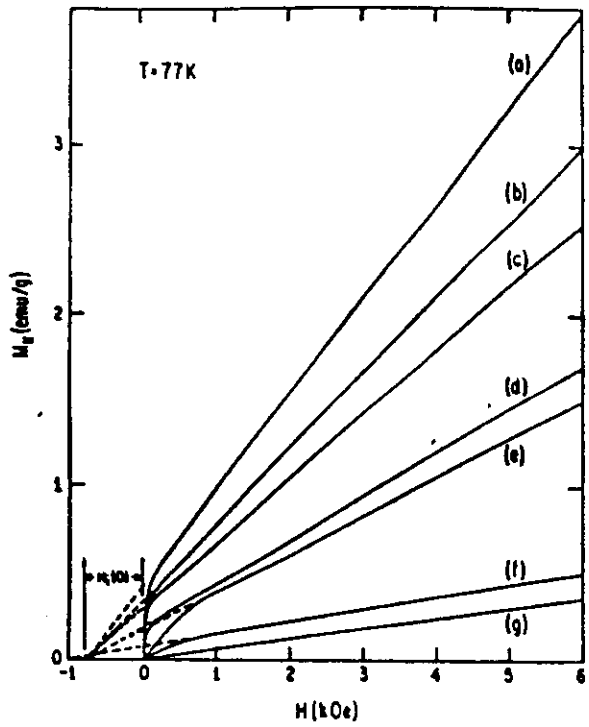

FIG. 4. The dc magnetization, M_{dc}, vs magnetic field applied parallel to the a-b plane for the following compounds at a temperature of 77 K: (a) $GdTbCuO_4$, (b) $EuTbCuO_4$, (c) Gd_2CuO_4, (d) $EuGdCuO_4$, (e) $SmGdCuO_4$, (f) $Eu_{1.8}Gd_{0.2}CuO_4$, and (g) Pr_2CuO_4. The linear dependence at higher fields corresponds to the paramagnetism of the R ions. When extrapolated back to zero M_{dc}, all the lines but the one for Pr_2CuO_4 intersect near a reverse field, $H_i(0) = 800$ Oe.

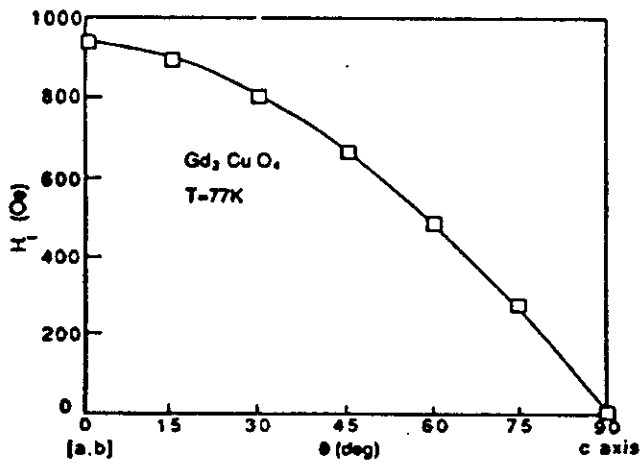

FIG. 6. The internal field H_i for Gd_2CuO_4 at 77 K, obtained by extrapolating to zero magnetization once the linear region in the magnetization has been established, is given as a function of angle of the applied field to the CuO_2 planes. The solid line corresponds to the best fit to $H_i(\theta) = H_i(0)\cos\theta$ with $H_i(0) = 930$ Oe. The $\cos\theta$ dependence arises because we only measure the component of M_{dc} in the direction of the applied field, as discussed in the text.

S. Oseroff et al., Phys. Rev. B 41 (1990) 1934

$H_r(\theta) = H_0 - H_1(\theta)\cos\theta + K'_1\cos\theta$

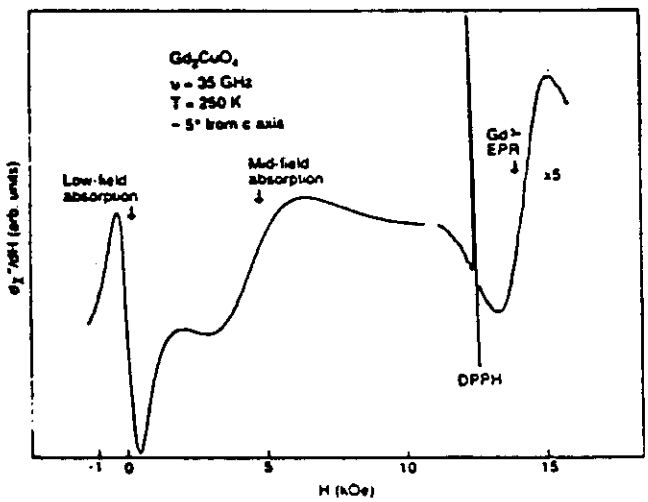

FIG. 17. Spectrum for a 0.3 mg single crystal of Gd_2CuO_4 measured at 250 K and 35 GHz with the field applied ~5° from the c axis, so the low-field absorption, midfield absorption, and Gd^{3+} EPR signals are all resolved. The DPPH is used as a marker. Notice the substantial shift from $g=2.00$ for the Gd^{3+} EPR line.

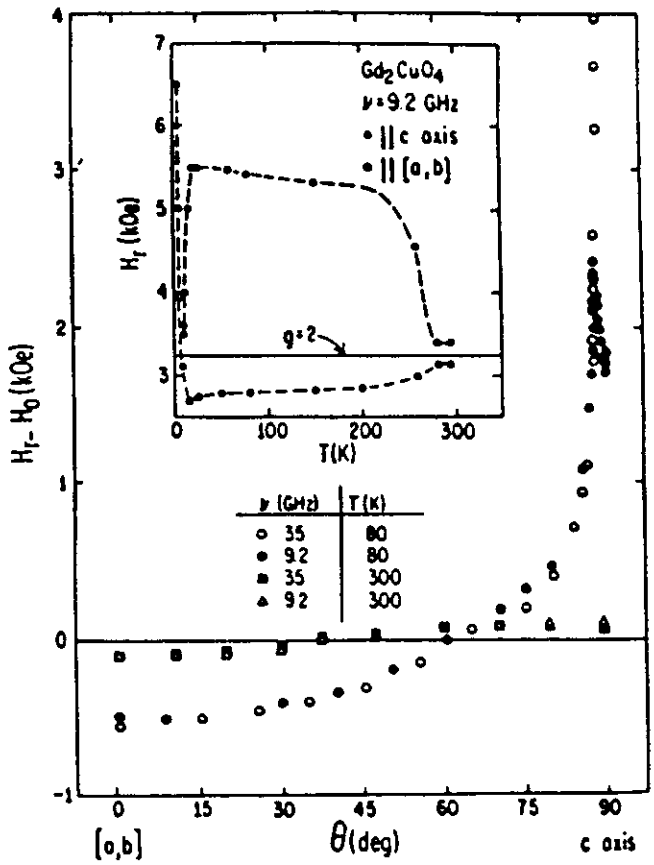

FIG. 18. The field shift of the EPR of the Gd^{3+} ion in Gd_2CuO_4, relative to that for $g=2$, vs θ, the angle of the applied field relative to the a-b plane for the temperatures and frequencies indicated. Above 270 K, H_r is basically independent of angle, whereas below and down to ~19 K, there is the anisotropic behavior shown. Inset. H_r vs temperature for $\theta=0°$ and 90°. Note the rapid changes in H_r at temperatures near T_a and $T_\perp$.

S. Oseroff et al., Phys. Rev. B 41 (1990) 1934

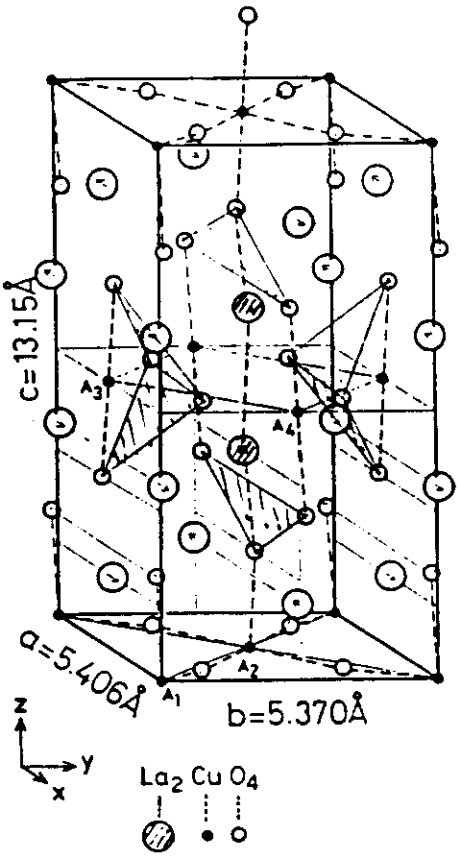

Fig. 1. The crystal structure of La_2CuO_4 (space group: Abma) from ref. 5. Arrows shown in the La and O sites indicate the directions of their displacements.

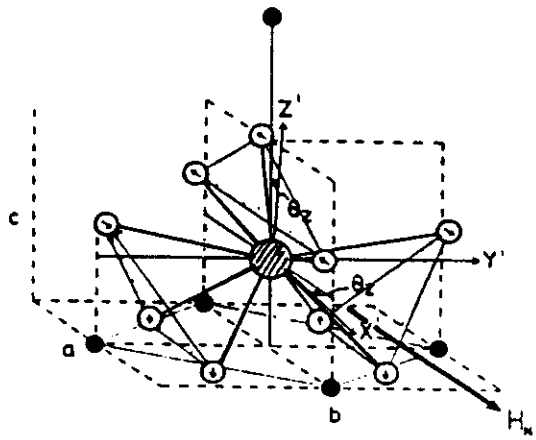

Fig. 9. Local arrangement of oxygen atoms around a lanthanum atom. The principal axes X, Y and Z of EFG calculated by the point charge model and the direction of the internal field H_N at the lanthanum site are shown (see text). Arrows show the directions of the displacements of the oxygen atoms.

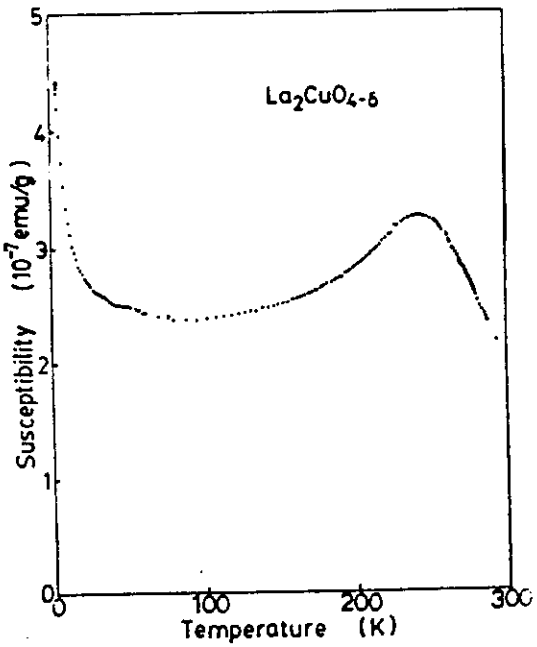

Fig. 2. Temperature dependence of magnetic susceptibility of $La_2CuO_{4-\delta}$ in a static field of 11.8 kOe.